Promoting Influence of Doping Indium into $BaCe_{0.5}Zr_{0.3}Y_{0.2}O_{3-\delta}$ on the Chemical Stability, Sinterability and Electrical Properties

by

Guangya Wang

A thesis submitted in partial fulfillment of the requirements for the degree of

Master of Science

in

Chemical Engineering

Department of Chemical & Materials Engineering

University of Alberta

Abstract

The application of $BaCe_{1-x-y}Zr_xY_yO_{3-\delta}$ series solid proton conductors in SOFCs is restricted by the trade-off among the chemical stability, sinterability and electrical conductivity under SOFCs operating conditions. The present research attempted to enhance the chemical stability, sinterability and ensure the high electrical conductivity of $BaCe_{1-x-y}Zr_xY_yO_{3-\delta}$ by doping indium. $BaCe_{0.5-x}Zr_{0.3}In_xY_{0.2}O_{3-\delta}$ (where x = 0, 0.05, 0.1, and 0.2) powders were synthesized by a combustion method. The influence of the indium dopant on chemical stability, sinterability, and electrical properties of the sintered samples was investigated. Phase purity and chemical stability were evaluated by XRD. SEM images and a shrinkage plot showed that the sinterability of the samples was improved by the indium doping. The electrical conductivity was measured with an impedance test through a two-point method at both low (200–350 °C) and high (450–850 °C) temperature ranges in different atmospheres. $BaCe_{0.4}Zr_{0.3}In_{0.1}Y_{0.2}O_{3-\delta}$ showed the highest electrical conductivity (1.1×10^{-2} $S.cm^{-1}$) in wet hydrogen at 700 °C. An anode support fuel cell was fabricated by a spin coating method. A maximum power density of 651 mW/cm^2 was obtained when operating at 700 °C and fed by humid H_2 and the cell ran stably for more than 100 hours.

Keywords: indium, electrolyte, proton, solid oxide fuel cell.

Acknowledgements

I am deeply grateful to Dr. Jingli Luo for her supervision and guidance throughout this study. I am grateful to group members past and present— Tong Gao, Yifei Sun, Subiao Liu, Shaohua Cui, and Drs. Ning Yan, Xianzhu Fu, and Xinwen Zhou, for their meaningful, critical, and constructive comments and suggestions for this project. I sincerely appreciate the kind support of my daily life provided by Hongqiang Fan, Dahai Xia, and Chen Shen, who work in a different lab and direction from me. I thank technicians Weizhu An, Diane Caird, Shiraz Merali, Shihong Xu, Kevin Hdidebrecht, Walter Boddez, and Les Dean for their help in CO_2 gas, XRD, SEM, and instrument repair. I also feel grateful to the supervisors who worked with me in my undergraduate time, Drs. Shibin Wang, Aizheng Chen, Yuangang Liu, and Cheng Peng. Special thanks are due to the teachers who inspired all my life, Binqi Liu and Zhuo Wang. And this work was funded by Natural Science and Engineering Research Council of Canada (NSERC).

Above all, I thank my parents, my elder brother Shuitao, and little sister Zhen, who encouraged me to continue my studies to high levels. I appreciate the warming help and support from my girlfriend Mengmeng, especially when I was preparing for my defense. They gave me amazing life and taught me to struggle for better. Without their encouragement and inspiration, I would not be able to accomplish my thesis.

Table of Content

List of tables

List of figures

List of symbols and units

δ	number of reduced oxygen atoms in unit cell due to addition of dopant
^{o}C	degree Celsius
F	Faraday constant, 96485 C/mol
R	resistance
σ	conductivity
K	Boltzmann constant, $1.3806488(13)\times10^{-23}$ J/K
C	capacitance with unit of F
ω	frequency of alternating current
ε	dielectric constant
f	fugacity
$D_{10,\ 50,\ 90}$	represent particle size at the 10% (50%, 90%) point of the cumulative, undersize PSD, respectively.
Å	10^{-10} m
t	tolerance factor
R	resistor
Q	constant phase element
T	Kelvin temperature
Ea	activation energy

List of abbreviations

AFC	alkaline fuel cell
PEM	proton exchange membrane
MCFC	molten carbonate fuel cell
SOFCs	solid oxide fuel cells
PC-SOFCs	proton conducting solid oxide fuel cells
OC-SOFCs	oxygen ion conducting solid oxide fuel cells
CHP	combined heat and power
IC	internal combustion
PHEV	plug-in hybrid electric vehicles
SEM	scanning electronic microscopy
XRD	x-ray diffraction
TGA	thermal gravity analysis
TPB	triple phase boundary
PSD	particle size distribution
vol%	volume percent
wt%	weight percent
OCV	open circuit voltage
GHG	greenhouse gas

Chapter 1 Introduction

1.1 Background

1.1.1 Present world energy market

There is increasing demand for energy in the world market due to economic growth, especially in developing countries, and the increasingly energy-intensive lifestyle and trends that modern society embraces [1]. These demands pose a serious environmental sustainability challenge and there is much concern whether these competing needs can be satisfied by the shrinking fossil fuels. In recent decades, these considerations have intensified the search for energy sources that are reliable and sustainable [2]. Figure 1.1 shows how levels of world energy demand, the existence of renewable energy, and the finite energy decline are predicted to change from 2000–2050.

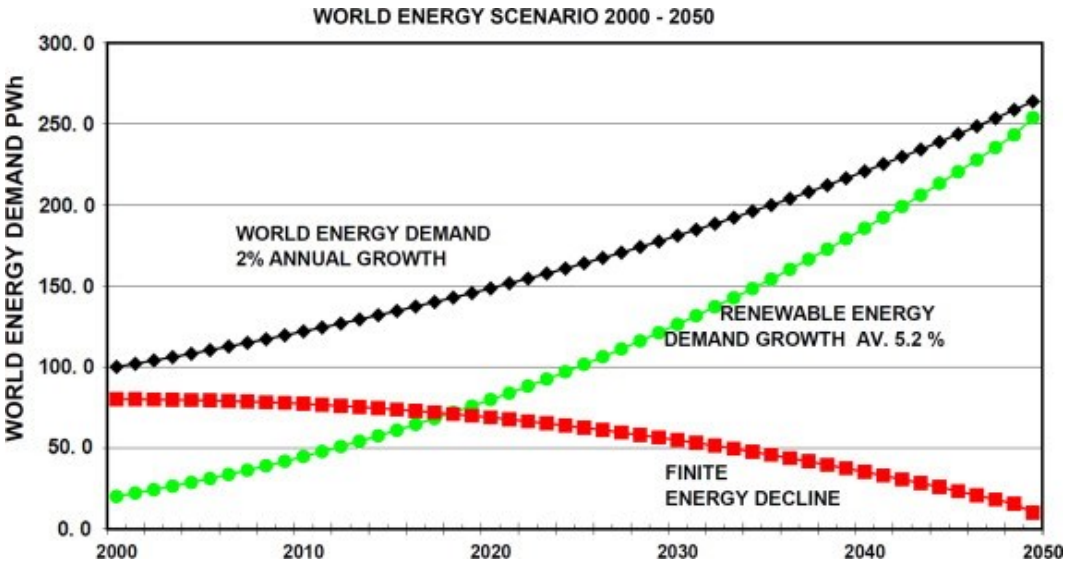

Figure 1.1 Plots showing the world energy scenario 2000–2050 [3].

With the rapid depletion of oil reserves, natural gas and coals are again being considered as alternative energy sources. However, to accomplish a long-term balance of energy demand-supply, it is essential to develop renewable energy resources (RESs) using wind, solar, and tidal energy systems. Electrochemical devices, represented by fuel cells, can play an important role in providing clean hydrogen gas for mobile applications and in efficiently converting fuel to electricity. One problem with the use of energy is its contribution to greenhouse gases which are warming the planet in a dangerous way. Three strategies can be considered to address energy needs and greenhouse gas (GHG) emissions: (1) energy losses can be minimized with efficient utilization of fossil fuels, (2) RESs can be developed to achieve their full capacity, and (3) green fuels, e.g., hydrogen and biofuels, can be utilized [2]. These strategies can be largely supplemented by the development of fuel cells, which are the most efficient way (efficiencies of 40–60%) to directly convert hydrogen to heat and power at the point of use for decentralized stationary power systems and for transportation. In addition to high efficiency, another advantage of fuel cells is their environmentally friendly operation; water is the only byproduct when hydrogen is used as fuel, and negligible or undetectable nitrous oxides are emitted.

1.1.2 Solid oxide fuel cells

Configurations and promising applications of solid oxide fuel cells (SOFCs) are illustrated in Figure 1.2 [4]. A typical configuration of a SOFC consists of the following components: two porous electrodes (a cathode and an

anode, which are catalysts for the electrochemical reactions), and an ion conductive electrolyte.

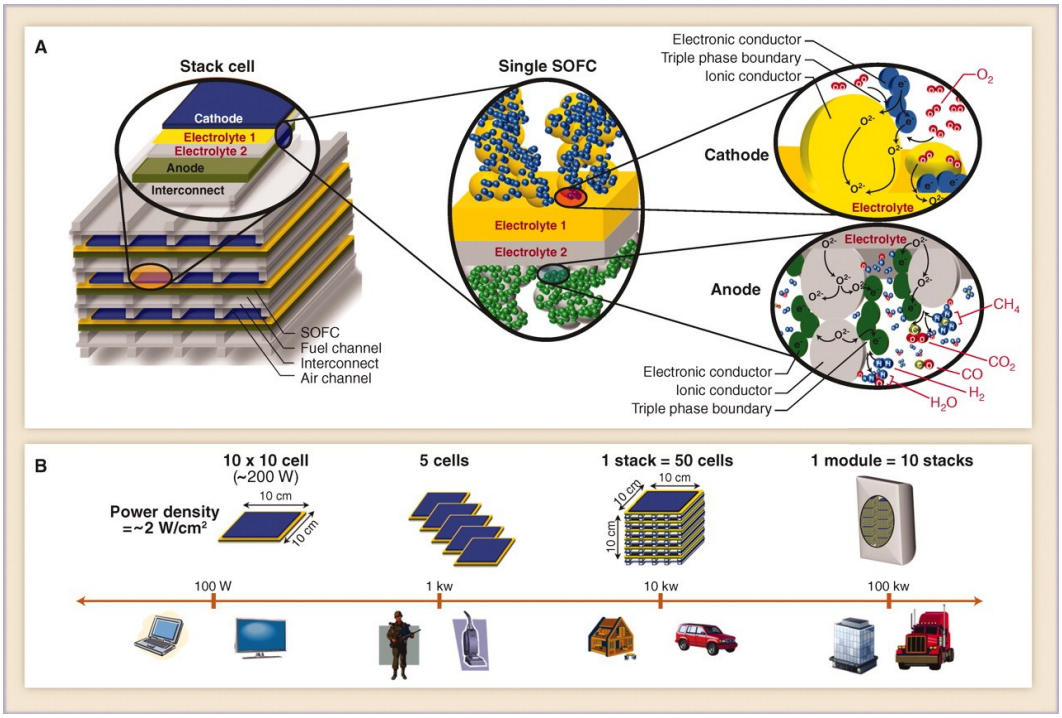

Figure 1.2 (A) Schematic diagram of SOFCs with different magnification from a unit stack cell to an anode-cathode microstructure. (B) Estimation of power output with SOFCs from a single cell to a module and a schematic diagram of power requirements according to various applications [4].

The electrolyte must have full densification and adequate chemical and thermal stability under the operating conditions. In oxygen ion conducting SOFCs, O_2 is reduced to O^{2-} at the cathode and the resulting oxygen ions are transported through the electrolyte to the anode, where O^{2-} reacts with a gaseous fuel, yielding heat, H_2O, and CO_2 (in the case of hydrocarbon fuels), at the same time producing electricity by releasing electrons (e^-) to an external circuit [4].

SOFCs are excellently stackable. As shown in Figure 1.2 B, multiple cells can be stacked via the interconnections which provide electrical contacts and gas channels between individual cells. Unit stacks can be further arranged in series and parallel configurations to provide more applicable voltage and power output from a mobile device (100 W), transportation applications (10 kW), to distributed generation (100 kW) and large-scale stationary power plants (> 1 MW), in both civilian and military sectors [5].

Compared with other types of fuel cells, e.g., proton exchange membrane (PEM) cells, direct methanol fuel cells (DMFC) and molten carbonate fuel cells (MCFC), one of the advantages of SOFCs is that they can be directly fed by flexible fuels (not only limited to hydrogen) usually produced from syngas (synthesis gas—a fuel gas mixture consisting primarily of hydrogen, carbon monoxide and very often, some carbon dioxide) or natural gas. In addition to fuel flexibility, SOFCs are 45–65% efficient in the conversion of fuel to electricity; such efficiency is unheard of in any other technology [5]. Considering the combined heat and power (CHP), which is the concept of simultaneous production of electrical and applicable thermal energy, the total system efficiency of SOFCs can exceed 85%, much higher than that of a thermo power plant or an internal combustion (IC) engine [5]. SOFCs are compared with other energy devices in Figure 1.3 [4]. For portable and transportation applications, volumetric and gravimetric power densities are a key performance standard. State-of-the-art SOFCs have a total thickness of 0.5 mm with an expected interconnect thickness of 1.5 mm [4]. Consequently, based on an area power density of 2 Wcm^{-2}, the

stack volumetric power density and the gravimetric power density are about 10 Wcm^{-3} and 3 $kWkg^{-1}$, respectively, exceeding that of an IC engine, as described in Figure 1.3 A [4]. In addition, with liquid hydrocarbon fueling, SOFCs have essentially the same specific energy (around 1 $kWhkg^{-1}$) as IC engines (Figure 1.3 B). Thus, it is reasonable to claim that SOFCs are potentially able to transform the automotive sector as a range extender for plug-in hybrid electric vehicles (PHEVs) operating on conventional fuels, since the corresponding 10 kW stack would be only a small cube of 10 cm per edge as shown in Figure 1.2 B [5].

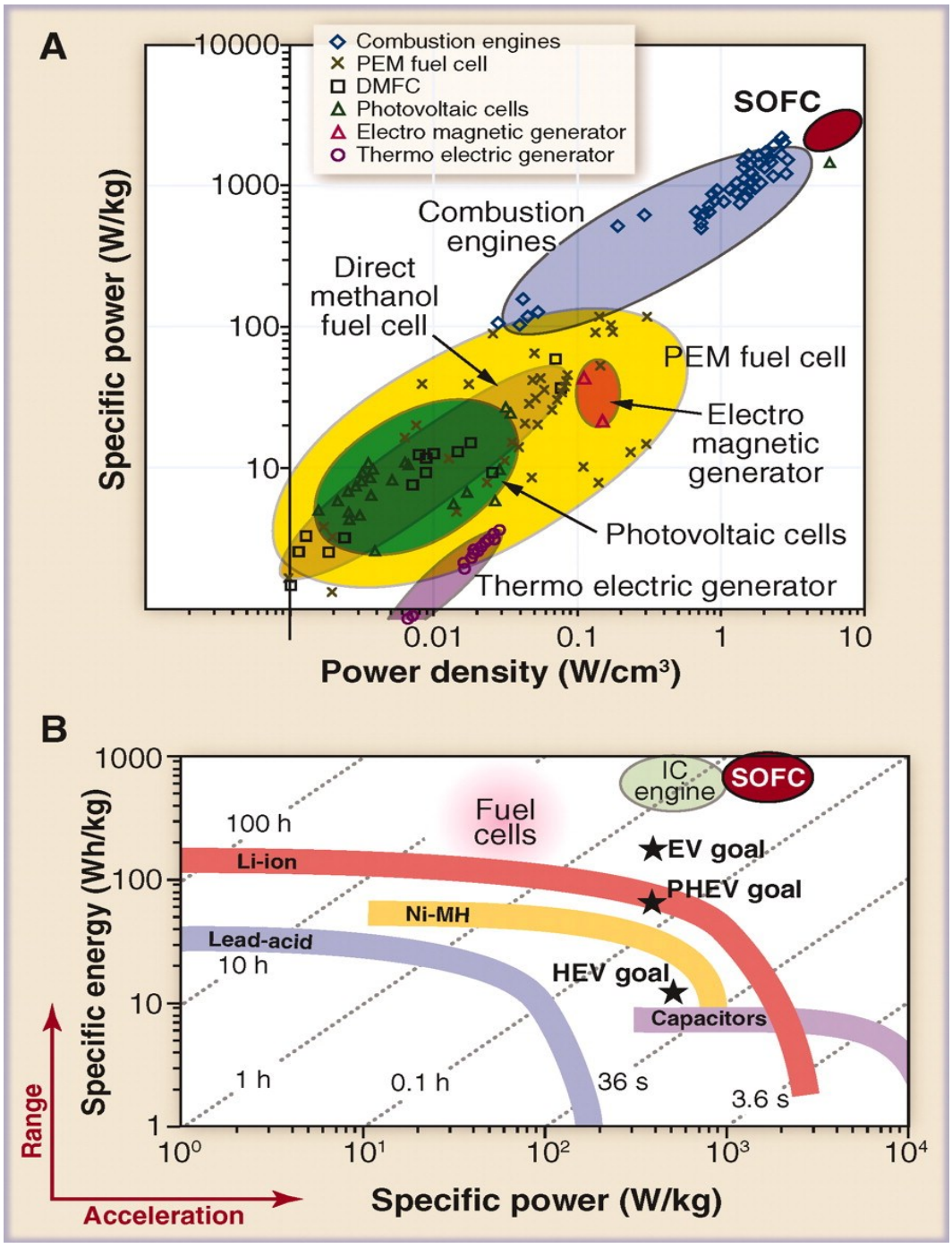

Figure 1.3 (A) Specific power vs. power density of current 2 Wcm^{-2} SOFC at 650 °C compared with various energy conversion devices with varying power densities [6]. (B) Ragone plot for various energy devices compared with current SOFCs [7].

1.1.3 Proton conducting SOFCs (PC-SOFCs)

Unlike oxygen ion conducting SOFCs (OC-SOFCs), proton conducting SOFCs (PC-SOFCs) use proton conductive materials as electrolytes. A schematic diagram of a typical PC-SOFC is shown in Figure 1.4. Under the catalytic function of the anode, protons can be generated from a hydrocarbon or a H_2 fuel gas. The resulting protons are transported via the electrolyte through a hopping mechanism to the cathode, where the protons react with O_2 to generate water and electricity is produced by the release of electrons to the external circuit. Unlike OC-SOFCs which generate water at the anode, PC-SOFCs generate water at the cathode, avoiding dilution and fluctuation of the fuel gas flow to improve the cell performance.

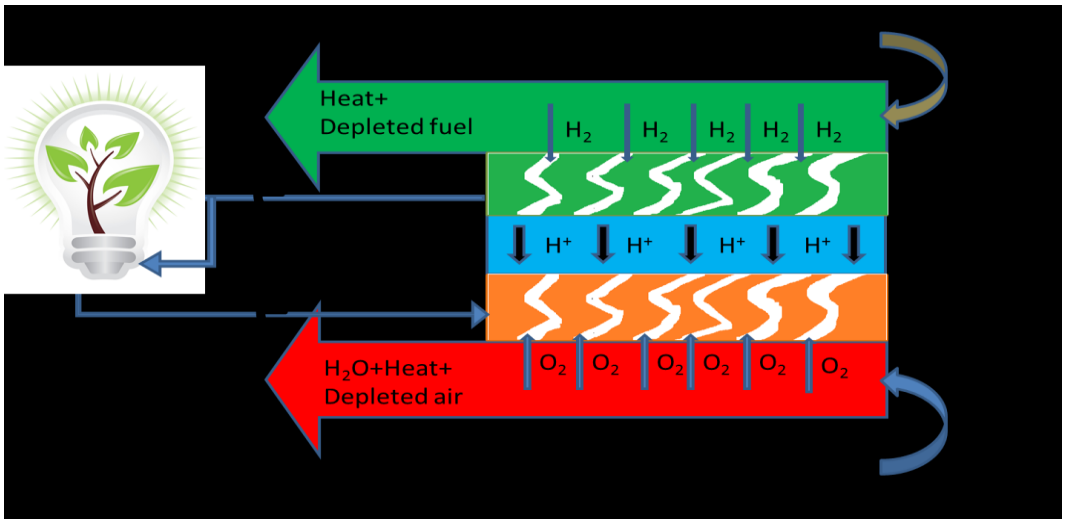

Figure 1.4 Schematic of the operation of a solid oxide fuel cell based on a proton conducting electrolyte.

PC-SOFCs have also been investigated as chemical reactors to co-produce electricity and products [8-10]. It is important that, due to the relatively low activation energy of proton conduction, the optimal operating temperature of a

PC-SOFC is in the range from 500 °C to 700 °C whereas OC-SOFCs based on yttria-stabilized zirconia (YSZ) can obtain maximum cell performance only above 850 °C. The relatively lower operating temperature can reduce the operating cost of fuel cells to some extent, and provides room for the selection and development of potential materials for electrodes, interconnectors and sealants [11].

The research achievements of PC-SOFCs are encouraging but still far from being satisfactory. The main limitations of PC-SOFCs lie in the lack of reliability and durability of electrolytes. The electrical conductivity of up-to-date proton conductors falls in the range of 10^{-2} to 10^{-1} Scm^{-1} in the temperature range of 500 °C to 700 °C [4]. The high electrical conductivity of a PC electrolyte is always offset by poor chemical stability in CO_2 and/or water vapour, which are common components of hydrocarbon fuel gas. In addition, sinterability significantly affects electrical properties of solid proton conductors. There is still much work to be done to boost cathode performance to an applicable level, and to discover suitable anode materials with efficient resistance to carbon deposition and sulfur poisoning during operation in natural hydrocarbon gas [8, 12-14].

1.2 Fundamental theories

1.2.1 Formation and mobility of proton defects

Figure 1.5 shows the ABO_3 perovskite structure. The B cation is usually a transition metal or a rare earth with +4 valence and forms a six-coordinated octahedron with its neighboring oxygen ions, being itself located in the center. The A cation generally has a larger ionic radius than the B catoin, presenting a +2 valence with coordination number of 12 [11].

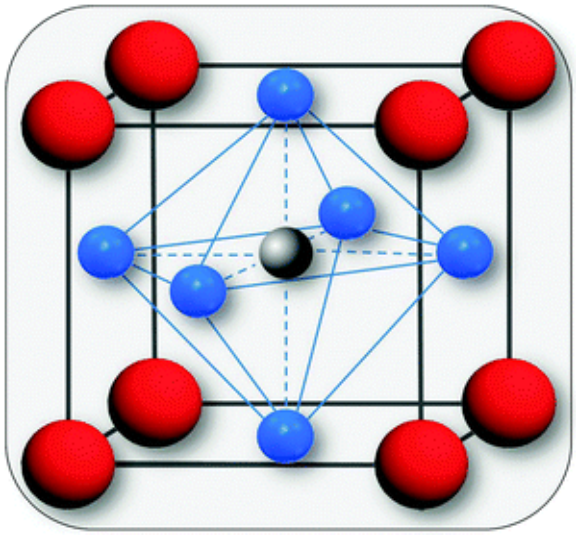

Figure 1.5 Perovskite crystal structure (ABO_3).

Oxygen vacancies in ABO_3 perovskite structure can be generated by substituting B^{4+} with trivalent cations M^{3+} (e.g. Y^{3+}, and In^{3+}), as denoted by Kroger-Vink notation:

$$2B_B^{\times} + O_O^{\times} + M_2O_3 \leftrightarrow 2M_B' + V_O^{\cdot\cdot} + 2BO_2. \quad (1.1)$$

Mobile protons can be incorporated into perovskite structure in the presence of water vapour and/or in the hydrogen containing gases. In a dry hydrogen atmosphere, the formation of hydroxide defects can be represented by:

$$H_2 + 2O_O^X \leftrightarrow 2(OH)_O^\bullet + 2e' \quad (1.2)$$

However, the more determining process for generating protonic defects is considered to be the dissociative adsorption of water, which can be presented as:

$$H_2O + V_O^{\bullet\bullet} + O_O^\times \leftrightarrow 2(OH)_O^\bullet \quad (1.3)$$

Water molecules dissociate into a hydroxide ion and a proton; the former occupies an oxygen vacancy while the latter can form a covalent bond with lattice oxygen. This dissociative adsorption process is exothermic, which explains why protons dominate conduction at low temperatures and oxygen vacancies dominate at higher temperatures [11].

According to equations 1.1 and 1.3, proton saturation is equal to the dopant concentration. However, the proton solubility limit was found to approach the dopant concentration only when the tolerance factor of perovskite oxide was close to unity [15]. Isotope effect experiments with proton conductors showed that the proton is conducted by proton hopping between adjacent oxygen ions at normal lattice sites via a Grotthuss-type mechanism.

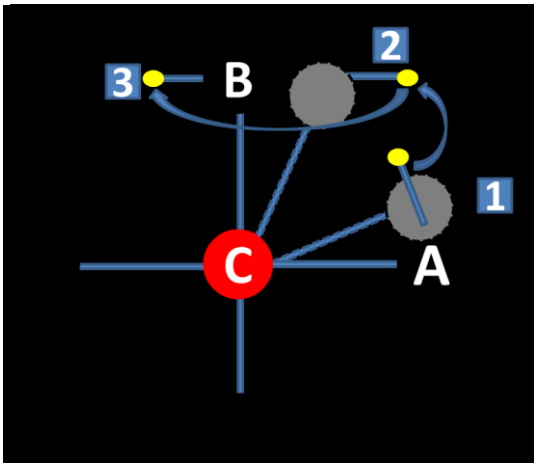

Figure 1.6 Sketch of a possible proton transfer mechanism from oxygen ion A to oxygen ion B in a perovksite oxide [11].

In Figure 1.6, for a proton to transfer from oxygen ion A to oxygen ion B, the bond between oxygen A and the center cation C must first bend, shortening the bond length between A and B and reducing the energy barrier for proton motion. Then, the bond between the proton and oxygen ion A will break, and a new bond between the proton and oxygen ion B will form (i.e., the proton will move from position 1 to position 2). After this process, the proton moves to position 3, likely by rotation around oxygen ion B. Repetition of the process described above generates the flow of proton conduction [11].

The incorporation of dopants can distort the structure of perovskite oxide, affecting the activation energy for proton conduction. Generally, larger distortion leads to higher activation energy of proton conduction. The local chemical perturbation induced by cation dopants can also affect the mobility of proton defects. Traditionally, to better tailor oxygen-ion conductors, aliovalent dopants were preferentially selected on the basis of ionic radius matching. However, this

rule occasionally fails for proton conductors because the electronic structure of dopants affects the electrical properties of proton conductors more than ionic radius matching [2]. P-type electronic conduction occurs as a result of oxygen incorporation that produces a hole as represented by:

$$O_2 + 2V_O^{\bullet\bullet} \leftrightarrow 2O_O^{\times} + 4h^{\bullet} \quad (1.4)$$

As the temperature increases, electrical conduction mainly occurs in the order of hydroxide ions, holes and oxygen vacancies. The temperature at which a certain conduction mechanism is dominant depends on the dopant content, the partial pressures of external oxygen/water vapour, and the Gibbs free energy change of all the involved reactions [16].

1.2.2 Alternating current impedance spectra

Electrochemical impedance spectroscopy (EIS) has proved to be a powerful tool to probe behaviors that contribute to cell performance. As shown in Figure 1.7, a low-amplitude harmonic current,

$$i_e(t) = \bar{i}_e + \hat{\imath}_e \sin(\omega t), \quad (1.5)$$

where ω is the transiting frequency, is applied to a single fuel cell (e.g., a button cell) and the corresponding harmonic cell voltage response,

$$E_{cell}(t) = \overline{E}_{cell} + \hat{E}_{cell} \sin(\omega t + \theta), \quad (1.6)$$

is generated with phase shift θ [17].

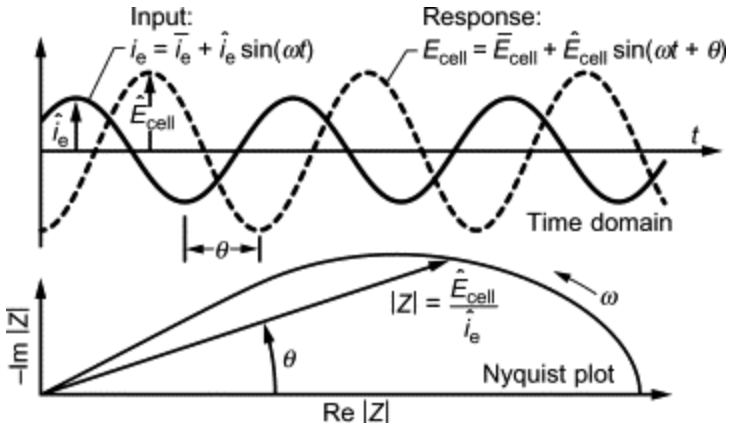

Figure 1.7 Qualitative illustration of electrochemical impedance spectra [17].

Phase shift θ and the ratio of $\hat{E}_{cell}/\hat{I}_e$ depend on the frequency and the nominal applying current $\bar{I}_e$. The corresponding complex impedance Z can be presented as:

$$Z = \frac{\hat{E}_{cell}}{\hat{\imath}_e} e^{-j\theta} = \frac{\hat{E}_{cell}}{\hat{\imath}_e}(cos\theta - jsin\theta), \tag{1.7}$$

where $j \equiv \sqrt{-1}$ [17]. For a given frequency, the complex impedance can be shown as a point on a Nyquist plot, as shown in Figure 1.7.

To more clearly isolate each individual contributing factor to the integrative cell performance, testing results of EIS are most commonly interpreted in the context of equivalent circuits using a combination of electronic elements, e.g., resistors and capacitors. Resistors usually represent ion transport processes and charge-transfer kinetics, while capacitors are usually associated with double-layer charging at the electrode-electrolyte interface together with transient effects of gas transport and chemistry [17, 18]. EIS plots usually consist of one or more arcs representing some aspects of the underlying physics or chemistry.

1.2.3 Electrochemical process in SOFCs

1.2.3.1 Thermodynamically predicted voltage

In terms of fuel cells where overall chemical reaction at constant temperature and pressure is :

$$\mathrm{A} + \mathrm{B} = \mathrm{C} + \mathrm{D} \qquad (1.8),$$

the generated Gibbs free energy change (ΔG) provides the maximum acquirable electrical work (W):

$$W = \Delta G = -nFE \qquad (1.9).$$

In equation 1.9, n is the number of electrons transferred in the reaction, F is Faraday's constant (96 485 C/mol), and E is the ideal potential of the fuel cell [2].

The Gibbs free energy change of reaction 3.8 can be represented by:

$$\Delta G = \Delta G^o + RT ln \frac{f_C^\gamma f_D^\delta}{f_A^\alpha f_B^\beta}, \qquad (1.10)$$

where ΔG^o is the Gibbs energy change of the reaction at the standard state pressure (1 atm) and at temperature T, R is the molar gas constant and f_i is the fugacity of species *i*. Combining equations (1.9) and (1.10) produces[2]:

$$E = E^o - \frac{RT}{nF} ln \frac{f_C^\gamma f_D^\delta}{f_A^\alpha f_B^\beta}. \qquad (1.11)$$

1.2.3.2 Voltage loss

The difference between the reversible cell voltage and the actual cell voltage is called over-potential, over-voltage or polarization and is denoted as η.

As shown in Figure 1.8, this over-potential can be mainly attributed to the following elements:

1) Activation loss is caused by the slowness of the reaction taking place on the electrodes' surface.

2) Fuel crossover and internal current. This voltage loss is brought about by a waste of fuel passing through the electrolyte and to a lesser extent, by electron conduction through the electrolyte.

3) Ohmic loss. To eliminate this loss, electrolyte as well as electrode materials are tailored to be more conductive. Another strategy is to reduce the thickness of the electrolyte [5].

4) Mass transport or concentration loss.

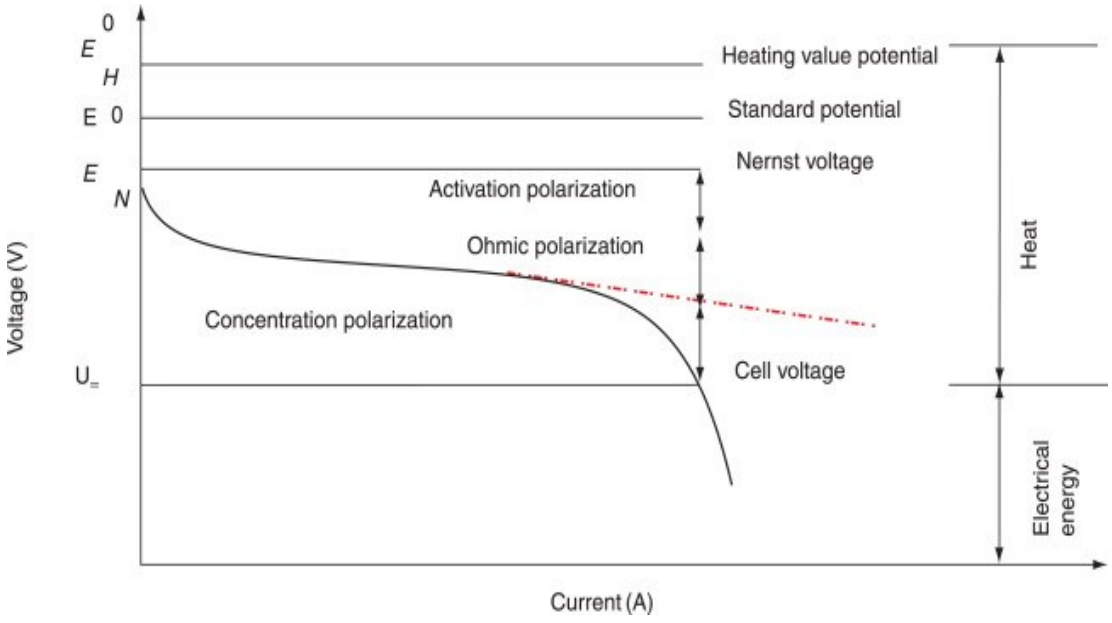

Figure 1.8 Schematic voltage-current (IV) curve [2].

As shown in Figure 1.8, with rising current, the ohmic loss increases and exhibits a proportional relationship with the current density over a wide range. Higher current density requires a larger species exchange rate at the reaction surfaces. If the exchange rate is insufficient, a marked reactant concentration gradient builds up and leads to concentration polarization.

1.3 Literature review

1.3.1 Solid oxide proton conductors in PC-SOFC applications

Proton conductivity of the electrolyte dominates the ohmic resistance in SOFCs, and thus has a large impact on comprehensive fuel cell performance. To optimize the cell performance, the electrolyte must be dense to avoid gas leakage and chemically/thermally stable in the operating conditions, especially when hydrocarbons are used as fuel. More importantly, the electrolyte should exhibit a desired proton conductivity in the required cell running temperature range, and contribute no more than 0.15 Ωcm^2 to the total cell resistance [4]. Furthermore, the electrolyte should be adhesive well with the electrodes or through the interconnectors. The most widely studied solid oxide proton conductors for PC-SOFC applications can be grouped in four series: complex perovksite (e.g., $Ba_3Ca_{1.18}Nb_{1.82}O_{9-\delta}$) [19], rare-earth orthoniobates (e.g., $LaNbO_4$) [20], fluorite related materials (e.g., $La_2Zr_2O_7$) [21], and the materials based on barium cerate and zirconate (e.g., $BaCe_{0.7}Zr_{0.1}Y_{0.2}O_{3-\delta}$).

1.3.2 Complex perovskite

The ideal perovskite oxides have a cubic crystal structure and a formula of ABO_3, where A and/or B sites contain mixtures of two or more different atoms in complex perovskite oxides. The general formulas of complex perovskite oxides are $A_2(B'B'')O_6$ and $A_3(B'B''_2)O_9$ [22]. The biggest advantage of complex perovskite oxide proton conductors is their excellent chemical stability in CO_2

and/or even boiling water. However, the low proton conductivity is a drawback considering the practical application of PC-SOFCs [11].

Valkenberg et al., reported that total resistance of $Ba_3Ca_{1.18}Nb_{1.82}O_{9-\delta}$ (BCN_{18}) was dominated by the grain boundary contribution, which suffered from an aging effect [23]. Nowick et al., found that when $x > 0$, $Sr_2(Sc_{1+x}Nb_{1-x})O_{6-\delta}$, was an oxygen ion conductor, but became an excellent proton conductor, with an activation energy of 0.63 eV, after pretreatment in water vapour [24]. Ta doped double perovskite type BCNs with the compositions of $Ba_2(Ca_{0.75}Nb_{0.59}Ta_{0.66})O_{6-\delta}$, $Ba_2(Ca_{0.75}Nb_{0.66}Ta_{0.59})O_{6-\delta}$, and $Ba_2(Ca_{0.79}Nb_{0.66}Ta_{0.55})O_{6-\delta}$ remained the same as prepared after pure CO_2 treatment at 800 °C for 7 days and boiling water treatment for 7 days, suggesting long term structural stability against chemical reactions. Among all samples tested, $Ba_2(Ca_{0.79}Nb_{0.66}Ta_{0.55})O_{6-\delta}$ provided the highest proton conductivity of 4.8×10^{-4} Scm^{-1} at 400 °C in wet H_2 (3 vol% H_2O) [25-27].

1.3.3 Rare-earth orthoniobates

Acceptor doped rare-earth orthoniobates with a general formula of $Ln_{1-x}M_xNbO_{4-x/2}$, (Ln = Y, La, Nd, Gd, Tb, Er, M= Ca, Sr, Ba, and $x \leq 0.1$) were found to be proton conductive and have acceptable chemical stability against CO_2 [28, 29].

Haugsrud et al., found that protons were the major charge carrier in $LaNbO_4$ in the presence of water vapour, with a maximum proton conductivity of about 0.001 Scm^{-1} at 950 °C for 1 mol% Ca doped $LaNbO_4$ in a wet atmosphere [28].

Ivanova et al. studied B site and A/B sites codoped lanthanum niobates, $La_{(1-x)}DA_{(x)}Nb_{(1-y)}DB_{(y)}O_{(4-\delta)}$, where DA stands for Ca or Ba while DB for Ga, Ge, or In (x = 0 or 0.01; y = 0.01). A maximum conductivity of 4.1×10^{-4} Scm^{-1} at 900 °C was obtained for $La_{0.99}Ca_{0.01}Nb_{0.99}Ga_{0.01}O_{4-\delta}$, about 2.5 times lower than the highest conductivity reported for the A site Ca doped $LaNbO_4$ [15]. For $La_{1-x}Sr_xNbO_{4-\delta}$ ($0 \leq x \leq 0.02$), $La_{0.995}Sr_{0.005}NbO_{4-\delta}$ possessed the highest conductivity (0.003 Scm^{-1}) in humid 5% H_2 (balanced with Ar) atmosphere at 800 °C with an activation energy of 0.44 eV [28, 30]. Similar to complex perovskite oxides, acceptor doped rare-earth orthoniobates showed the desired chemical stability in CO_2 and/or water vapour containing gas. However, the overall electrical conductivity was about one order of magnitude lower than that of barium cerates and zircoante [31].

1.3.4 Pyrochlore/fluorite type solid proton conductor

Pyrochlore type oxides have a general formula $A_2B_2O_7$, where A site atoms (La, Nd, Sm, Eu, Gd, Y, Yb) have a valence of 3+ and B sites can be occupied by 4+ cations, e.g., Zr, Ce, Ti, or Sn. Pyrochlore can be considered as a derivative of fluorite. The two structures fall into space group Fd-3m and Fm-3m, respectively.

In 1997, electrochemical pumping of oxygen was used to demonstrate that $La_2Zr_2O_7$ based materials possess a significant protonic conductivity contribution at temperatures lower than 1000 °C. The results also revealed that substitution of Y for Zr enhanced the electron holes, oxygen ions, and protonic conductivity contribution [32]. $La_{1.95}Ca_{0.05}Ce_2O_{7-\delta}$ (LCCO), synthesized by the Pechini method, showed excellent chemical stability against CO_2 with 3 vol% H_2O at 700 °C [33].

Under wet hydrogen atmosphere, pure proton conduction was observed below 600 °C in both $La_{2-x}Ca_xZr_2O_{7-\delta}$ and $La_2Zr_{2-x}Ca_xO_{7-\delta}$ systems. The proton conductivity of $La_{1.95}Ca_{0.05}Zr_2O_{7-\delta}$ at 600 °C in wet H_2 was 6.8×10^{-4} Scm^{-1} [34].

1.3.5 Doped barium cerates and zirconates

Solid proton conductors based on acceptor-doped barium cerates and zirconates have been intensively researched. Barium cerates and zirconates follow the typical perovksite formula ABO_3, with Ba^{2+} at the A site and Zr^{4+} or Ce^{4+} at the B site. Similar to other compounds described above, oxygen vacancies can be formed in the perovskite structure by charge balance due to incorporation of trivalent dopants at the B site. Hydration of these doped barium cerates and zircoantes takes place when they are treated in atmospheres containing water vapour, through which protons can be incorporated into the oxygen vacancies in the form of hydroxide ions. Proton conduction occurs via a Grotthuss-type mechanism, transferring the proton from one oxygen ion to an adjacent one [11].

Generally, barium cerates possess high electrical conductivity but vulnerable chemical stability, while barium zirconates are adequately stable in CO_2 and/or H_2O containing gas; however, the electrical conductivity of barium zirconates is relatively lower than barium cerates due to the large grain boundary. To obtain a larger grain size, barium zirconates have to be sintered at super high temperature (> 1600 °C) for a prolonged time (> 15 h) [35], resulting in not only high energy consumption but alsoelement evaporation. Solid solutions of barium cerates and barium zirconates can be obtained due to their mutual solubility over the whole composition range. This composite compound system is expected to

combine advantages (excellent chemical stability and good electrical conductivity) derived from the two parent materials. Furthermore, doping or codoping into solid solutions of barium cerate and zirconate has been performed to better balance the trade-off between electrical conductivity and chemical stability.

Table 1.1 give a summarization of the electrical conductivity and chemical stability of the representative $BaCe/ZrO_3$ based proton conductors. As shown in table 1.1, the electrical conductivity of these representative proton conductors lies in the range of 10^{-3} to 5×10^{-2} Scm^{-1}.

Table 1.1 Summarization of the most representative $BaCe/ZrO_3$ based proton conductors

Materials composition	Conductivity/Scm^{-1}	T/^oC	CO_2 content (v%), treating time (hours), temperature (^oC)	H_2O content/v%
$BaCe_{0.95}Gd_{0.05}O_{2.975}$	1.87×10^{-3}	650	pure, 5, 650	3 [36]
$BaCe_{0.87}Nb_{0.03}Y_{0.1}O_3$	1.01×10^{-2}	650	pure,5,700	3 [37]
$BaZr_{0.7}Sn_{0.1}Y_{0.2}O_3$	1.6×10^{-3}	600	3%,10,600	Boiling [38]
$Ba_{1-x}Sr_xCe_{0.6}Zr_{0.2}Y_{0.2}O_3$	0.9×10^{-2}	800	Ambient air,5, 600	3 [39]
$BaCe_{0.85-x}Zr_xSm_{0.15}O_3$	5×10^{-3}	700	3%, 5, 600	3 [40]
$BaCe_{0.9}Y_{0.1}O_3$	0.8×10^{-2}	650	10%, 10, 700	No [41]
$BaZr_{0.8}In_{0.2}O_3$	1×10^{-3}	700	15%, 8, 650	3 [42]
$BaCe_{0.8}Gd_{0.15}Pr_{0.05}O_3$	7.6×10^{-3}	600	Pure, 5, 750	3 [38]
$BaCe_{0.6}Ta_{0.3}Y_{0.1}O_3$	0.94×10^{-2}	750	10%, 600	3 [43]
$BaCe_{0.65}In_{0.3}Ti_{0.05}O_3$	7×10^{-3}	750	3%,7, 700	No [44]

1.3.5.1 Proton conductivity

The proton conductivity of perovskite solids is theoretically determined by the concentration and mobility of proton defects, which can be significantly

affected by the type and concentration of dopants. In 1999, Ryu et al. investigated the proton conductivity of compounds with general formula $BaCe_{0.9-x}Zr_xM_{0.1}O_{3-\delta}$, where M is Gd or Nd and x ranges from 0 to 0.4 as determined by AC impedance spectroscopy in dry and H_2O saturated argon. As expected, introduction of Zr led to a decrease in conductivity and an increase in the activation energy for proton transport. Overall, Nd-doped samples exhibited higher chemical stability and lower conductivity than those doped with Gd. The composition of $BaCe_{0.7}Zr_{0.2}Nd_{0.1}O_{3-\delta}$ appeared to give a good compromise between conductivity and stability for fuel cell applications [41]. Almost at the same time, Katahira et al. synthesized Zr-substituted $BaCeO_3$ ($BaCe_{0.9-x}Zr_xY_{0.1}O_{3-\delta}$) and characterized it for proton conductivity. Single phases were confirmed over the whole range of x values ($0.0 \leq x \leq 0.9$). These oxides exhibited pure protonic conduction in hydrogen-containing atmosphere and showed protonic, oxide ionic, and electronic mixed conduction under high oxygen partial pressure at elevated temperatures [45]. Concentration cell tests of $BaZr_{0.4}Ce_{0.4}In_{0.2}O_3$ (BZCI) revealed good proton conductivity in hydrogen-rich atmosphere and that BZCI behaved as a protonic and oxide ionic conductor in oxygen-rich atmosphere, with some electronic conductivity, which lowered its ionic transport number. At the same time, a single cell Pt\BZCI\Pt produced power with an open circuit voltage (OCV) of 1.02 V at 600 °C with humid H_2 as fuel [46]. In 2006, Zuo et al. reported a new $BaZr_{0.1}Ce_{0.7}Y_{0.2}O_{3-\delta}$ ($BCZY_7$) which provided an electrical conductivity of around 2×10^{-2} Scm^{-1}. $BCZY_7$ gained remarkable attention and was widely used as a proton conductive electrolyte by other researchers [12, 47-52]. A fuel cell with Ni

as anode and $BCZY_7$ as electrolyte produced a maximum power density of above 250 $mWcm^{-2}$ at 700 °C with humid H_2 as fuel [53]. However, other studies indicated that the Zr concentration of 0.1 may not lead to an adequate chemical stability [45, 50, 54].

A paper by Yang et al. published in Science reported the preparation and characterization of a novel proton conductive material, $BaZr_{0.1}Ce_{0.7}Y_{0.1}Yb_{0.1}O_{3-\delta}$ (BZCYYb), which exhibited high ionic conductivity of around 6×10^{-2} Scm^{-1}, three times larger than that of $BCZY_7$. A single cell with the configuration Ni-BZCYYBb/BZCYYb/BCZYYb-LSCF gave a maximum power density of about 1.1 Wcm^{-2} at 750 °C with humid H_2 and air as fuel and oxidant, respectively [55]. A BZCYYb electrolyte prepared by ammonium carbonate coprecipitation displayed electrical conductivities of 1.9×10^{-2} Scm^{-1} at 500 °C and 7.4×10^{-2} Scm^{-1} at 750 °C with an activation energy of 0.45 eV. An anode support fuel cell with a BZCYYb electrolyte assembled by spin coating provided maximum power densities of 1.0 Wcm^{-2} at 750 °C and 0.23 Wcm^{-2} at 500 °C [56]. Differences between the experimental results of different researchers might be ascribed to each unique processing.

In 2011, Fabbri et al. synthesized 10 mol% Pr doped $BaZr_{0.8}Y_{0.2}O_{3-\delta}$ (BZPY), which offered a proton conductivity of above 10^{-2} Scm^{-1} at 600 °C in wet H_2 atmosphere. Electrochemical impedance spectroscopy (EIS) analysis performed during the fuel-cell tests under OCV conditions confirmed the good electrical performance of BZPY [57]. Recent (2011–2013) efforts to develop novel solid proton conductors based on doped barium cerates and zirconates

yielded conductivity values of 5×10^{-3} to 5×10^{-2} Scm^{-1} at temperatures 500–700 °C in wet H_2 containing atmospheres [8, 12, 41, 46, 48, 51, 53, 58, 59].

1.3.5.2 Chemical stability

One of the major advantages of SOFCs is the efficient utilization of hydrocarbon gas as fuel with CO_2, H_2O and H_2S as the common components. Thus, adequate chemical stability in this sour fuel gas is a necessity for proton conductors. The main drawback of $BaCeO_3$ is its high basicity which lowers the chemical stability. In CO_2 and/or H_2O containing atmospheres, $BaCeO_3$ decomposes due to the carbonation reaction:

$$BaCeO_3 + CO_2 \rightarrow BaCO_2 + CeO_2 \quad (1.12)$$

Dopants with smaller ionic radii and larger electronegativity than Ce^{4+}, e.g., Zr, Ta, Sm and Gd, can enhance the chemical stability of $BaCeO_3$. However, incorporation of lower basicity dopants (Zr, Ta, Gd) lowers the electrical conductivity. Therefore, the quest for dopants that can deliver chemical stability without much sacrifice in electrical conductivity is ongoing.

Ryu et al. investigated the chemical stability of $BaCe_{0.9-x}Zr_xM_{0.1}O_{3-\delta}$, (M is Gd or Nd; x= 0 - 0.4) through TGA and XRD analyses. The introduction of Zr into doped barium cerate greatly enhanced the chemical stability.In the Nd-doped system, compositions with x = 0.2 or higher did not react with CO_2 (under experimental, nonequilibrium conditions), whereas in the Gd-doped system, compositions with x = 0.4 did not react. Overall, Nd-doped samples exhibited

higher chemical stability and lower conductivity than samples doped with Gd [41]. Fabbri et al. synthesised $BaCe_{0.8-x}Zr_xY_{0.2}O_{3-\delta}$ (with $0.0 \leq x \leq 0.8$) proton conductor powders by a soft chemistry route. To verify the chemical stability, all the synthesized oxides were exposed to 100% CO_2 at 900 °C for 3 h. XRD revealed that the chemical stability against CO_2 increased with increasing Zr content. Specifically, when $x \geq 0.5$, samples survived the carbonation reaction [50]. The carbonation resistance of $BaCe_{1-x-y}Zr_xY_yO_{3-\delta}$ (x = 0, 0.10, 0.20, 0.30, 0.40; y = 0.15, 0.20) was evaluated by varying concentrations of Zr and Y [60]. Stability tests demonstrated that the introduction of Zr into doped barium cerate greatly enhanced the chemical stability, particularly when Zr ≥ 20%. Overall, $BaCe_{1-x-y}Zr_xY_yO_{3-\delta}$ solid solutions having 20–40% Zr and 15–20% Y showed good chemical stability and high conductivity [60]. The concentration of Zr necessary to maintain the perovskite structure in the BZCY series was lower than that found by Fabbri et al. [50]. Yang et al. reported that $BaZr_{0.1}Ce_{0.7}Y_{0.1}Yb_{0.1}O_{3-\delta}$ showed good chemical stability against CO_2 as well as 100 ppm H_2S [55]. More interestingly, a high electrical conductivity was simultaneously obtained [55, 56].

The chemical stability of Sm and Zr co-doped $BaCe_{0.85-x}Zr_xSm_{0.15}O_{3-\delta}$ (BCZS) ($0.01 \leq x \leq 0.3$) in H_2O vapour and CO_2 was tested [40]. All BCZS samples were found to be structurally stable against reaction with pure CO_2 at 400 °C for 24 h, showing a positive role of Zr in providing chemical stability. However, at 600 °C for 24 h, $BaCO_3$ was formed in BCZS when $0 < x < 0.2$ but not when x = 0.3 at 20% CO_2 in N_2. When exposed to H_2O vapour at 90 °C, $Ba(OH)_2 \cdot xH_2O$ formation was observed in all BCZS samples, whereas at 600 °C,

all impurity peaks in XRD spectra were invisible. Indium doping was also found to effectively enhance the barium cerate based proton conductors [44, 58, 61, 62].

1.3.5.3 Sinterability

Usually, solid proton conductors based on $BaZrO_3$ are chemically stable.However, their practical application is restricted by poor sinterability, which causes large grain boundary resistance and reduces the electrical conductivity. To increase the grain size, $BaZrO_3$ based electrolytes need to be annealed for a prolonged time at high temperature, consuming both time and energy. More importantly, critical sintering conditions tend to reduce the porosity of electrodes in fuel cells with electrode supported configurations, where electrolyte densification follows electrode fabrication.

Several doping strategies have been applied to improve the sinterability of $BaZrO_3$ based electrolyte materials. Tao et al. reported that the shrinkage of $BaZr_{0.8}Y_{0.2}O_{3-\delta}$ can be better achieved by doping with 1 wt% ZnO. Both doped and blank samples started shrinking at about 1000 °C However, with the addition of ZnO, shrinkage was found to be accelerated and notably, a second, faster sintering mechanism initiated just below 1300 °C. The total shrinkage of Zn doped BZY was 15.7% after being isothermally held at 1450 °C for 4 h, while shrinkage for blank BZY through the same treatment was 1.76% [63]. A more detailed research concerning the effect of sintering aids was reported in 2011 [64]. Polycrystalline powders of $BaCe_{0.9}Ln_{0.1}O_{3-\delta}$ (Ln = La, Nd, Sm, Gd, Yb, Tb, Y) were mixed with a nitrate solution containing the sintering aids Co, Zn, Ni, Fe, or Cu. Dense ceramic pellets were obtained by sintering at around 1000 °C instead

of approaching to or above 1400 °C. The addition of small amounts of transition metals did not produce structural changes observable by conventional X-ray powder diffraction. However, sample bulk and total conductivity decreased compared with samples without transition metals. Zn was the most effective sintering element for $BaCe_{0.9}Ln_{0.1}O_{3-\delta}$ electrolytes because it did not cause significant changes in ionic and electronic conductivities [64]. The effect of zinc oxide as a sintering aid on proton migration across a $BaZrO_3$ super cell with a ∑(310)/[001] tilt grain boundary was investigated using density functional theory. The result revealed that protons were trapped by high energy barriers in the range of 1.28–1.49 eV near zinc ions that substituted for Zr ions at the grain boundary. However, away from the zinc ions there were available pathways for proton migration across the grain boundary with relatively low energy barriers in the range of 0.61–0.78 eV. This might explain why the zinc ion located at the grain boundary did not affect the energy barrier for proton migration, although the number of mobile protons could decrease as a result of being trapped near the zinc ions [63-65].

1.3.5.4 Thin membrane fabrication

To optimize the cell performance of PC-SOFCs, it is essential to reduce the ohmic resistance of the electrolyte. Generally, two strategies can accomplish this goal. The first is to develop novel proton conductive electrolyte materials and the second is to reduce the thickness of the electrolyte. Traditional electrolyte supported fuel cells have relatively thick (> 500 μm) electrolyte membranes, fabricated by directly pressing the green powder into a pellet followed by high

temperature sintering. Electrode supported fuel cells take advantage of the enlarged reaction surface on electrodes. This allows a reduction in the thickness of the electrolyte membrane to 10–20 μm, which can be prepared by spin coating, co-pressing and tape casting. Novel thin (< 10 μm) membrane fabricating technologies, e.g., pulsed laser deposition (PLD) [66-69], chemical vapour deposition (CVD) [70-72] and atomic layer deposition (ALD) [73], have been utilized in SOFC research. A thin film of 0.5% Ca doped $LaNbO_4$ with a thickness of 2 μm was obtained by PLD. The film was densified by sintering at 1300 °C for 3 h and showed an area specific resistance of 0.4 Ωcm^2 at 600 °C in 3 vol% H_2O containing H_2 [74]. Chao et al. investigated a freestanding 10 nm thick YSZ electrolyte fabricated by ALD. The reduced thickness permitted a maximum power density of 1.34 Wcm^{-2} at temperatures as low as 500 °C [75]. Although there have been quite a few applications of these techniques on solid oxide proton conductors, practical applications are restricted by their high cost and complex operating processes [73].

1.3.6 Challenges, philosophy and objectives

One of the main advantages of PC-SOFC is the capability of utilizing the low cost hydrocarbon, in which sour compositions such as CO_2 and H_2S always exist. In PC-SFOC, water is produced at cathode, avoiding the fluctuation of fuel gas at anode. Due to the lower activation energy of proton conduction, PC-SOFC runs at an intermediate temperature range from 500 ^oC to 700 ^oC.

Lack of suitable proton conducting electrolytes is the bottleneck for development of PC-SOFC. Therefore, the main task is to discover the solid

proton conductors which possess adequate chemical and thermal stability in CO_2 and/or H_2O containing atmosphere, and high proton conductivity in the operating temperature range.

Among the candidates for solid proton conducting electrolytes, the most promising series are yttrium doped solid solution of $BaCeO_3$ and $BaZrO_3$ ($BC_{1-x}Z_xY_y$). From 500 ^oC to 700 ^oC, when $x \geq 0.5$, $BC_{1-x}Z_xY_y$ can maintain perovskite structure in pure CO_2, while x that is less than 0.3 can lead to almost complete decomposition of $BC_{1-x}Z_xY_y$ [36, 40, 41, 48-50, 53, 60]. $BC_{1-x}Z_xY_y$ with $x \geq 0.3$ needs an annealing temperature higher than 1650 ^oC to get full densification [45, 46, 50, 53, 60]. In order to balance chemical stability and sintering activity, molar content of Zr was set at 0.3. According to equations 1.1 and 1.3, higher concentration of Y results in more proton defects and in turn, benefits proton conductivity. Therefore, *y* was set at 0.2, which is the solubility limit of Y in solid solution of $BaCeO_3$ and $BaZrO_3$. Thus, $BaCe_{0.5}Zr_{0.3}Y_{0.2}O_{3-\delta}$ (BCZY) was selected as a parent material for a doping strategy in the present work. Pauling electronegativity of In is 1.78, higher than that of Ce (1.12) and that of Zr (1.33) [44, 76]. Therefore, In is expected to enhance the chemical stability of BCZY. In addition, In has been reported as an ideal sintering aid [42, 44, 61, 76]. Apart from this, valence and coordination number of In with oxygen in perovskite are 3 and 6, respectively (same as Y). It is reasonable to assume that In can exhibit synergistic effect with Y on increasing the concentration of oxygen vacancies in BCZY. Consequently, In was selected as the dopant for BCZY.

The objectives of the present study are to:

1. Enhance the chemical stability of BCZY,

2. Improve the sintering activity of BCZY,

3. Maintain high proton conductivity of BCZY by incorporating In.

Chapter 2 Preparation and characterization of perovskite powders

2.1 Introduction

The preparation procedure can significantly affect the properties of the powders, including surface morphology, particle size distribution, grain size, grain boundary width and porosity. Additionally, different materials' processes can introduce impurities to the product. Consequently, electrical properties will be influenced by the various preparation procedures since electrical conductivity is highly dependent on the properties of initial powders.

Solid state method is one of the most widely used methods to prepare ceramic powders because it is simple, highly scalable and results in large yields. However, in order to obtain the pure perovskite phase or ensure high ionic conductivity, powders or pellets produced through solid state method need repeated milling and calcination at high temperatures, which may result in contamination by impurity and element evaporation, respectively. The incorporated impurities may be piled up at the grain boundary and block the ion conduction, thus reducing electrical conductivity [77]. Also, in the solid state method, a multiphase reaction occurs in the materials interface, during which the rate-limiting step is ions' diffusion between different phases. This step is dominated by several uncertain factors. As a result, the composition and structure of the powders prepared by the solid state method always shows nonstoichiometry and inhomogeneity, which may further induce crystalline distribution and undermine the ions' conduction [77].

In recent years, a novel combustion synthesis process has been developed to produce ultrafine oxide ceramic powders with optimized powder properties in an extremely reduced reaction time at a lower calcination temperature. Characteristics of the powders, including crystalline size, surface area and nature of agglomeration, can be primarily governed by the enthalpy of the flame temperature generated during combustion, which is dependent on the nature of the fuel and the fuel-to-oxidant ratio [12]. Heat generated in the combustion process can be rapidly dissipated by the drastic evolution of a large volume of the gaseous products, limiting the temperature increase and reducing the possibility of premature local partial sintering among the primary particles. Additionally, gas evolution also helps to suppress the inter-contact of particles and thereby results in a more easily fireable product. In the combustion method, amino acids (e.g., glycine (NH_2CH_2COOH)) are always used as a complexing agent for numerous metal ions since amino acids have carboxylic groups and amino groups at two ends, respectively [40]. Fu et al. reported a modified citric acid-nitrates combustion method, which was used in the present work [10].

2.2 Experimental section

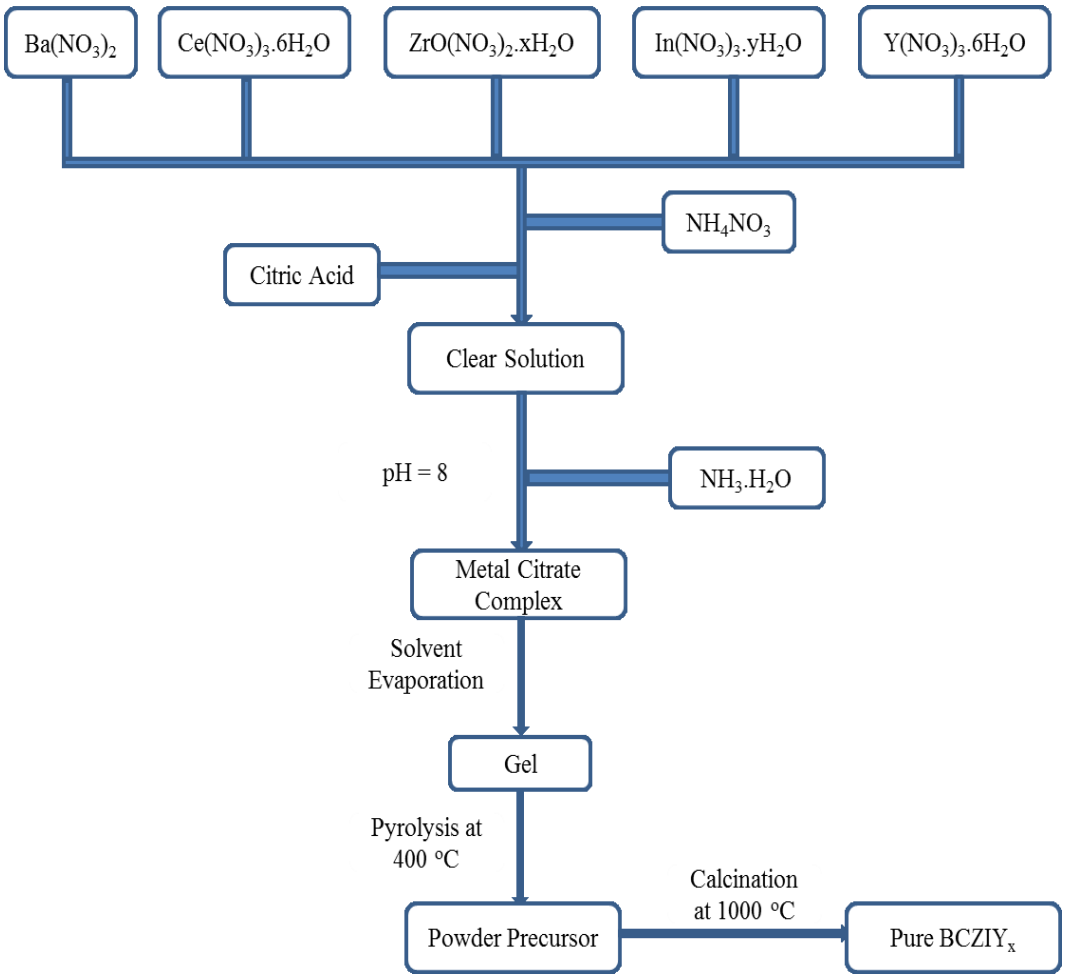

Figure 2.1 Process diagram of modified combustion method to prepare $BCZIY_x$ perovskite powders

Figure 2.1 illustrates the process diagram for preparing $BCZIY_x$ powders. $BaCe_{0.5-x}Zr_{0.3}In_xY_{0.2}O_{3-\delta}$ ($BCZIY_x$, x=0, 0.05, 0.1, 0.2) powders were prepared using a modified combustion method. Stoichiometric amounts of $Ba(NO_3)_2$ (Alfa Aesar, 99+%), $Ce(NO_3)_3 \cdot {}_6H_2O$ (Alfa Aesar, 99.5%), $ZrO(NO_3)_2 \cdot xH_2O$ (Alfa Aesar, 99.9%), $In(NO_3)_3 \cdot yH_2O$ (Aldrich, 99%), and $Y(NO_3)_3 \cdot 6H_2O$ (Alfa Aesar, 99.9%) were first dissolved in deionized water. X and y are crystal water numbers, determined by athermal gravity analysis (TGA) tests. Subsequently, citric acid

(Alfa Aesar, 99.5%) and NH_4NO_3 (Aldrich, 99.5%) were added as chelating agent and oxidant, respectively. The molar ratio of citric acid to total metal ions to NH_4NO_3 was 1.5: 1: 3. The pH of the resulting solution was adjusted to about eight using ammonium hydroxide (Acros, 28-30% NH_3 in water), and the solution was heated on a hot plate. After the water evaporated, the residue foamy gel self-ignited to form fine powders. Then the combusted powders were calcined at 950 °C for 10 h in air to form the pure perovsikte phase. A $Ba_{0.5}Pr_{0.5}CoO_{3-\delta}$ (BPC) cathode catalyst was synthesized via a similar technical route.

The surface morphological examination of the samples was performed using a field emission scanning electron microscope (FE-SEM, S-4800, HITACHI, Japan). Before observation, the samples were dispersed by ultrasound in ethanol suspension. The suspension was directly dropped onto an aluminium stub with a thin self-adherent carbon film and coated with a thin layer of gold. The particle size and particle size distribution of the samples were analyzed by Smileview from the SEM microphotographs.

The phase purity of synthesised $BCZIY_x$ powders was identified using a Rigaku Rotaflex X-ray diffractometer (XRD) with Co Kα radiation from 20 º to 110 º with a step of 0.01 º and the data were analyzed using JADE software. To evaluate the effect of In and Zr doping on the chemical stability of orginal $BaCe_{0.5}Zr_{0.3}Y_{0.2}O_{3-\delta}$ (BCZY), samples of different series ($BCZIY_x$, with x=0, 0.05, 0.1 and 0.2) were synthesised and treated in humid pure CO_2 (containing 3 vol% of H_2O) at 700 °C for 15 hours. After the test, XRD was used to investigate the composition changes of each sample. For shrinkage behavior measurements,

around 0.2 g of the obtained perovskite $BCZIY_x$ powders were uniaxially pressed into a short bar (with diameter of 3 mm and height of 2 mm) at 100 MPa for 30 seconds. Shrinkage tests of the $BCZIY_x$ sample bar were conducted by LINSEIS L75 Vertical Dilatometer (Germany) from room temperature to 1550 °C with a ramping rate of 10 °C /min. The final temperature was held for 30 min.

2.3 Results and discussion

2.3.1 Powder morphology and particle size distribution

The chelating power of citric acid promoted the uniformity of distribution of the metal ions and affected the powder morphology [10, 60]. The combustion method favored the formation of fine powders which could form perovskite structures at a lower calcining temperature than the solid state method. The prepared powders had a peanut-like morphology with a uniform distribution and the mean particle size of around 100 nm, as shown in Figure 2.2.

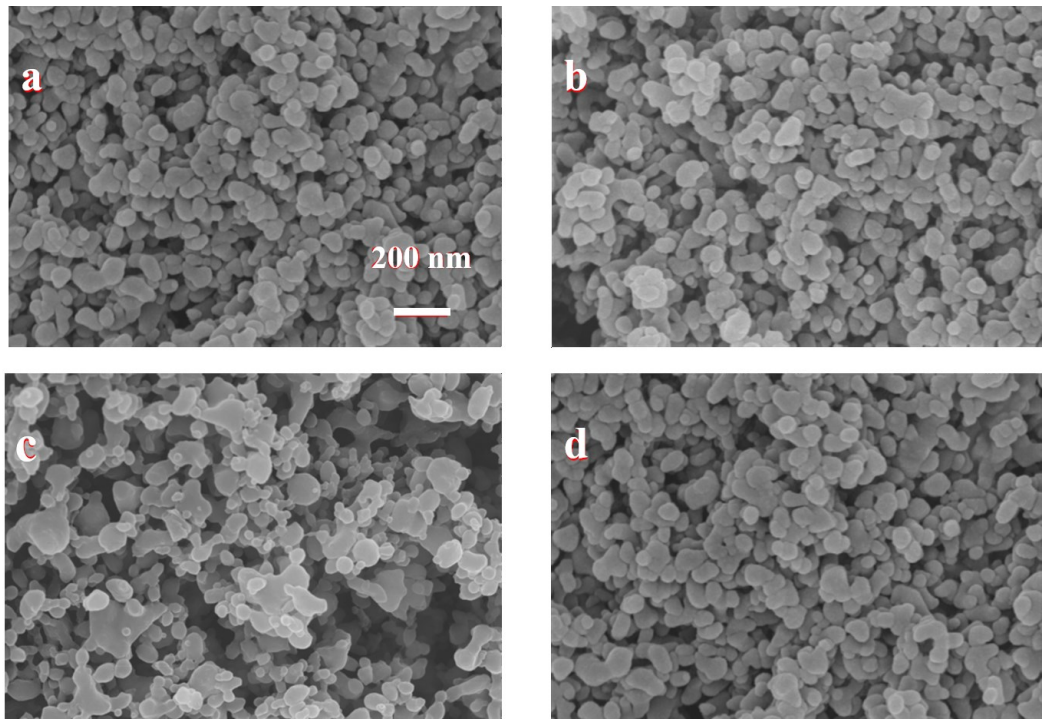

Figure 2.2 SEM image of perovskite powders of $BCZIY_x$ (x=0, 0.05, 0.1, 0.2) synthesized by citric acid-nitrate combustion method. (a)x=0; (b)x=0.05; (c)x=0.1; (d)x=0.2.

The width of particle size distribution (PSD) was evaluated by a span value, defined as:

$$Span = \frac{D_{90}-D_{10}}{D_{50}}; \tag{2.1}$$

where D10, D50 and D90 represent particle size at the 10%, 50% and 90% point of the cumulative, undersize PSD, respectively. The PSDs were summarized in Table 2.1. All samples exhibited a mean particle size of around 100 nm, with a monosized PSD (span ≤ 0.8). No remarkable difference was detected in any of the samples.

Table 2.1 Particle size distribution of $BCZIY_x$ (x=0, 0.05, 0.1, 0.2)

In content	D_{10}(nm)	D_{50}(nm)	D_{90}(nm)	Span	Mean size (nm)
0	52	79	110	0.73	96
0.05	61	81	123	0.76	110
0.1	55	91	108	0.58	105
0.2	63	89	115	0.58	99

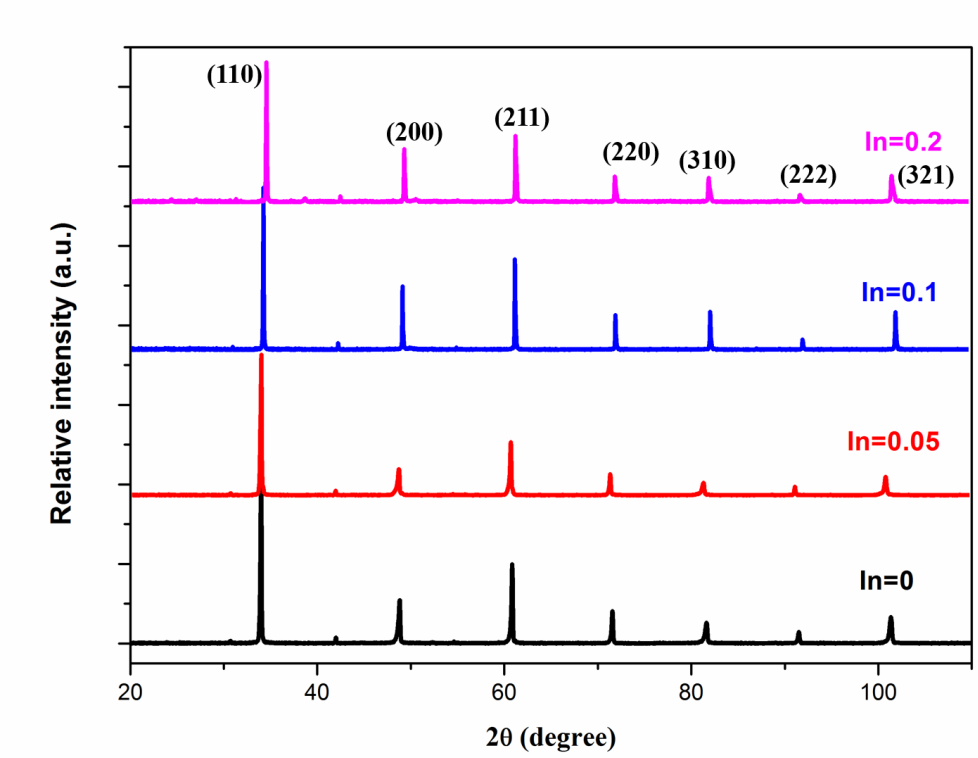

Figure 2.3 XRD pattern of perovskite powders of $BCZIY_x$ (x=0, 0.05, 0.1, 0.2) synthesized by citric acid-nitrate combustion method.

Figure 2.3 shows the XRD patterns of the $BCZIY_x$ (x=0, 0.05, 0.1, 0.2) series of powders sintered at 950 °C for 10 hours. All materials showed the typical perovskite structure index. No impurity peaks corresponding to single metal oxides were detected, indicating that all the elements were successfully

incorporated into the perovskite structure. Besides, little noticeable structural variation occurred in any of the samples; the only exception was the slight right shift of peaks in XRD spectra resulting from the substitution of Ce^{4+} (0.87 Å, 6-coordination with oxygen) with the smaller In^{3+} ions (0.8 Å, 6-coordination with oxygen), which was in agreement with the results in references[50, 60].

2.3.2 Phase purity and distortion measurement

XRD patterns were analyzed by the Rietveld method using the structural models previously proposed in the literature (ICSD 72768) in the orthorhombic Pmcn space group [54]. In order to evaluate the effect of incorporating In into the crystal structure distortion, a modified Goldschmidt tolerance factor of typical ABO_3 perovskite was defined and shown in the following equations:

$$t = \frac{r_A + r_O}{\sqrt{2}(\overline{r_B} + r_O)} \tag{2.2}$$

$$\overline{r_B} = \sum y_{B_i} r_{B_i} \tag{2.3}$$

where y ($0 \leq y \leq 1$) denotes the molar content of the B site element and r_A, and r_B (r_{Bi}) represent the radii of ions occupying A and B sites, respectively, while the oxygen ion radius is expressed as r_o.

Lattice parameters obtained by cell refinement using Jade software and tolerance factors were summarized in Table 2.2. In Figure 2.4, unit cell volume and tolerance factors of $BCZIY_x$ compounds were plotted against the In content. It is obvious that both the unit cell volumes, and tolerance factors showed linear dependence on the In doping content, which was considered as typical behavior for solid solutions [78]. Pure $BaCeO_3$ has a tolerance factor of 0.8568 [79] while

pure $BaZrO_3$ has a cubic perovskite structure, space group Pm3m, with a tolerance factor close to unity [60]. As for the $BCZIY_x$ solid solution, the tolerance factors increased as expected with increasing concentration of In, due to the smaller ionic radius of In^{3+} compared with Ce^{4+}, indicating the progressively reduced lattice distortion.

Table 2.2 Lattice parameters and unit cell volumes of calcined $BCZIY_x$ series samples

In content	Lattice parameters (Å)			Unit cell volume ($Å^3$)	Tolerance factor
x	a	b	c	V	t
0	6.009	8.543	6.121	303.24	0.8717
0.05	5.971	8.535	6.105	301.20	0.8731
0.1	5.942	8.505	6.098	299.67	0.8745
0.2	5.868	8.472	6.058	297.36	0.8772

It is generally accepted that lower cell lattice distortion from an ideal cubic perovskite structure leads to lower activation energy of ionic conduction [78]. However, it is the electronic structure of the dopant, in addition to the ionic radius matching, that mainly affects the proton conductors' electrical properties [11] This accounts for the fact that, in spite of the near ideal cubic structure, In doped BCZY has lower electrical conductivity compared with the parent materials. More details will be discussed in the following electrical properties section. Although increasing the In^{3+} content resulted in a higher concentration of oxygen vacancies which would, to some extent, expand the unit cell volume [64],

reducing ionic radii by increasing the In content had a greater impact on changing the lattice volume, thus leading to a downtrend of the cell volume.

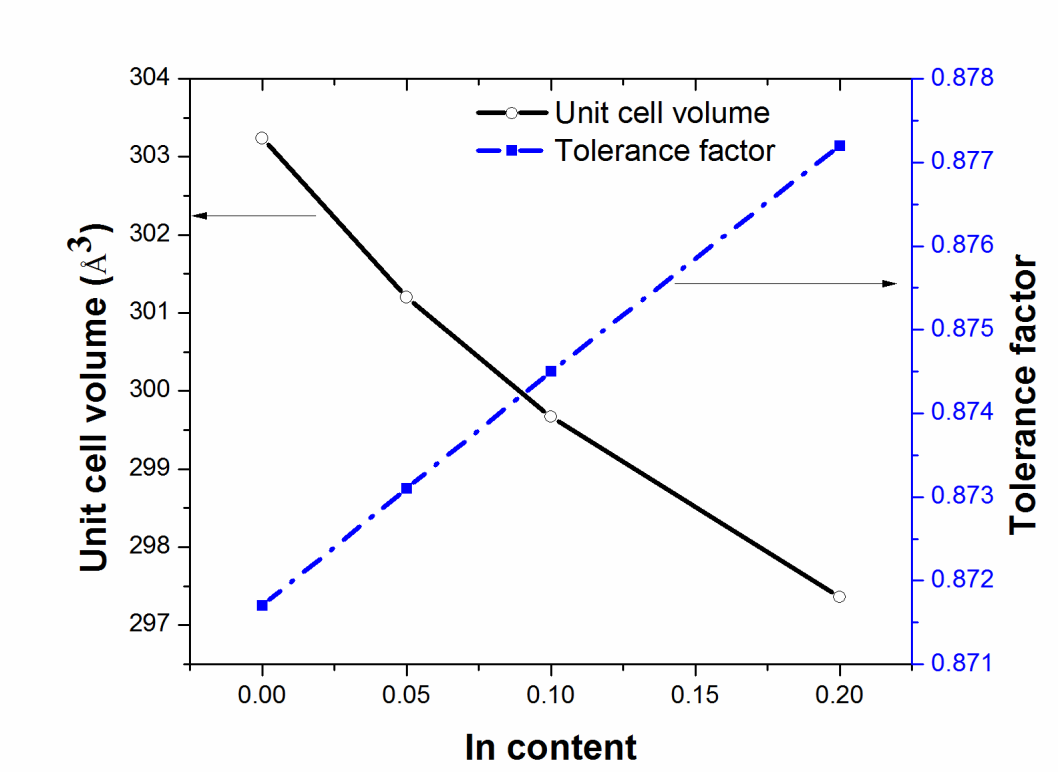

Figure 2.4 Variation of unit cell volume and tolerance factor with In content

One advantage of PC-SOFCs is that it can consume hydrocarbon fuel, not limited to pure hydrogen. Hydrocarbon gas can be in-situ reformed into CO_2 and H_2 under the catalytic process of PC-SOFCs anode [39]. H_2O is the product generated at the cathode. Thus, it is essential for the proton conductive electrolyte to exhibit sufficient chemical stability in CO_2 and/or H_2O containing atmosphere. This is especially important for anode support fuel cells because the thickness (10-20 μm) of the electrolyte is considerably reduced.

For a barium cerate and zicornate solid solution, the conventional way to improve the chemical stability is to increase the molar ratio of zirconium, at the cost of reduced sinterability, a larger grain boundary volume and remarkably decreased electrical conductivity. In this work, In was selected as the dopant to be added into $BaCe_{0.5}Zr_{0.3}Y_{0.2}O_{3-\delta}$ to improve the chemical stability and sinterability without significantly sacrificing the electrical conductivity.

Figure 2.5 shows the XRD patterns of BCIZYx powders of different composition before and after being treated with humid pure CO_2 (plus 3 vol% of H_2O) at 700 °C for 15 hours. Before the test, $BCZIY_x$ powders were calcined 950 °C for 10 hours to form pure perovskite structured as discussed above. In humid CO_2 containing gas, barium carbonate and cerium oxide may be extracted from the original perovskite oxide due to the following reaction:

$$BaCeO_3 + CO_2 \rightarrow BaCO_2 + CeO_2 \qquad (2.4)$$

As can be seen in Figure 2.5, before the chemical stability test, all $BCZIY_x$ compounds showed a well identified perovskite structure without impurity peaks. After the humid CO_2 treatment, additional peaks for barium cerate and cerium oxide can be observed for $BCZIY_x$ with x=0 and 0.05, as a result of the reaction between the tested compound and CO_2.

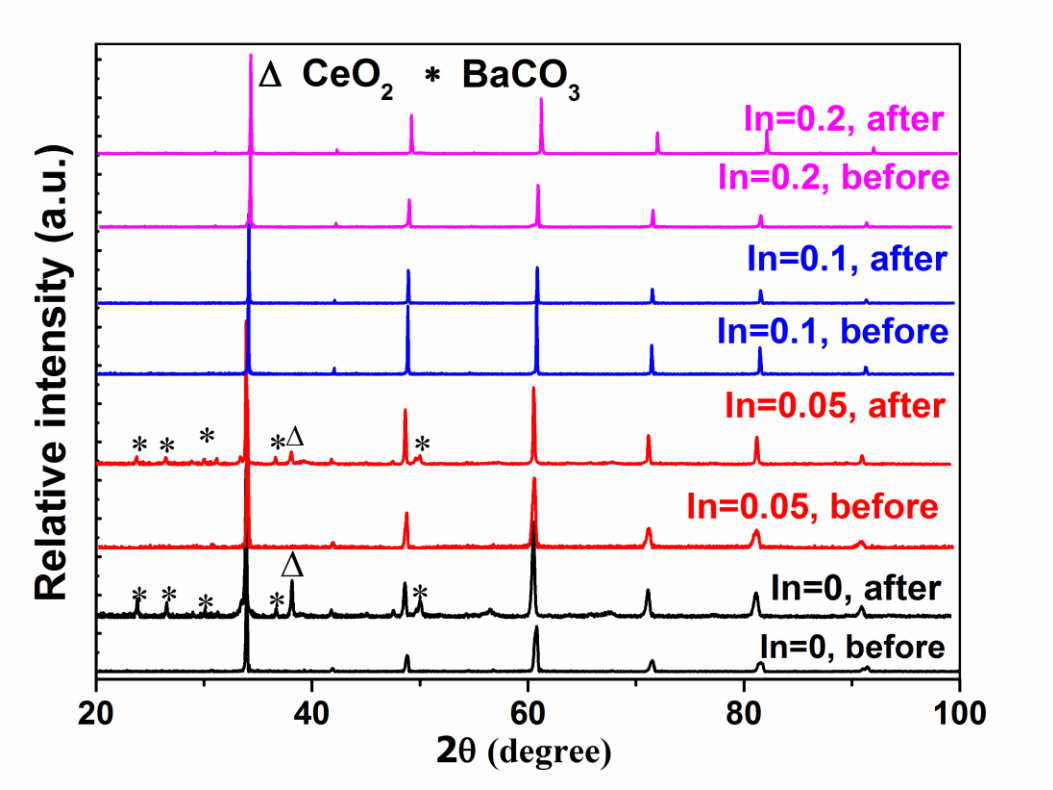

Figure 2.5 XRD pattern of $BCZIY_x$ (x=0, 0.05, 0.1, 0.2) powders before and after the chemical stability test.

Figure 2.6 is the magnified portion of XRD spectra within the dashed frame in Figure 2.5, and exhibits the existence of the faint but still detectable peaks for barium cerate and cerium oxide in the sample with In = 0.1, which may be due to the unavoidable carbonization reaction in the powder pile surface [42, 57].

In the case of In = 0.2, the impurity peaks completely disappeared. However, in terms of the harsh test condition (humid pure CO_2 at 700 °C for 15 hours), the chemical stability of $BaCe_{0.4}Zr_{0.3}In_{0.1}Y_{0.2}O_{3-\delta}$ was reasonably satisfactory. This result confirms that the chemical stability of indium-free BCZY was adequately enhanced by In doping, probably due to the relatively large electronegativity of In.

Similar phenomenon supporting the assumption has also been reported elsewhere [58, 62, 76, 80].

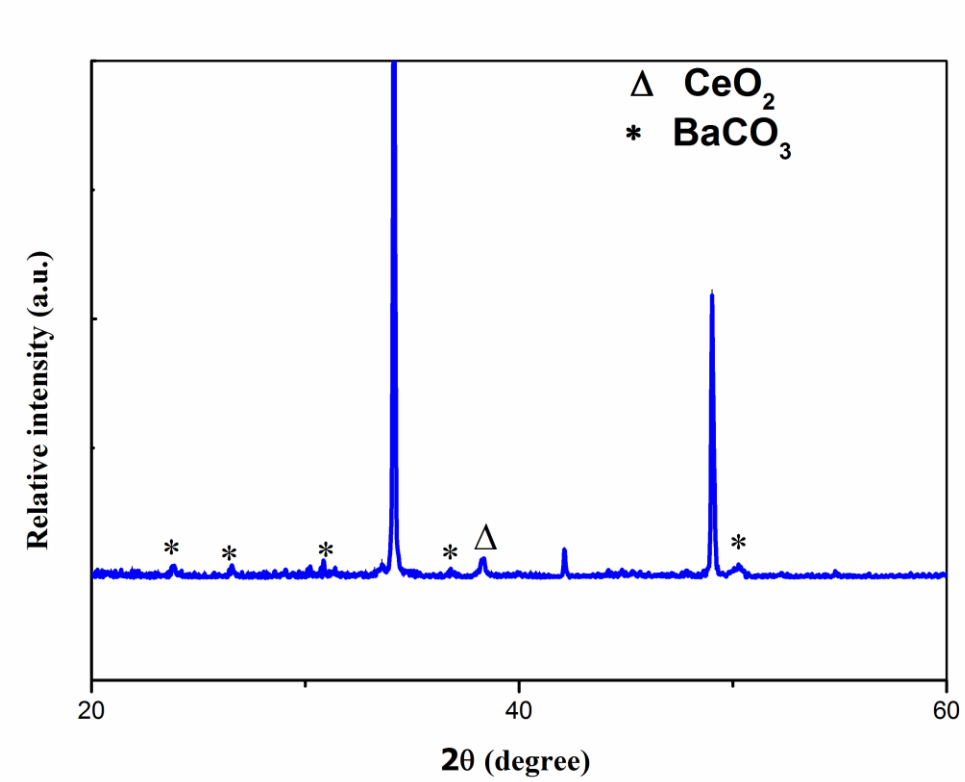

Figure 2.6 The magnified portion of Figure 2.5.

Chapter 3 Densification and characterization of pellets

3.1 Introduction

The most technically promising proton conductive electrolyte materials for intermediate temperature SOFC are those perovskites based on the cerates or zirconates of barium doped by yttria. These materials provide high protonic conductivity without remarkable contribution from oxide ions or electron conduction over a useful range of temperatures. Fundamentally, proton conductivity is determined by both the concentration and mobility of protons in perovksite oxides. Mobile protons can be incorporated into the perovskite structure as hydroxide defects in the presence of water vapor and/or in hydrogen containing gases. Research into isotope effects on perovksite oxides showed that protons are conducted by a hopping mechanism between adjacent oxygen ions at a normal crystalline lattice via a Grotthuss-type process [11]. Specifically, proton conduction between fixed oxygen ions occurs primarily by rotational diffusion of a proton around an oxygen ion, followed by a proton transfer toward a neighbouring oxide ion [11]. The types and concentration of dopant in zirconates and cerates of barium (or the solid solution) can lead to oxygen vacancies and crystalline structure distortion as well as chemical perturbation of the matrix, all of which work systematically to determine the actual proton conductivity [11].

The electrical conductivity of $BaZrO_3$ is much lower due to the presence of the large grain boundary surface caused by poor sinterability. To simultaneously combine the chemical stability and electrical conductivity in the best way, a series of solid solution of $BaCeO_3$ and $BaZrO_3$ with the addition of various dopants such

as indium [46], scandium [35], yttrium [53] and samarium [40] was developed and systemically researched. The perovskite structure of $BaCe_{1-x}Zr_xY_{0.2}O_{3-\delta}$ can be maintained only for these samples with $x \geq 0.5$ [50].

The zirconates do not sinter easily, and acceptable conductivities can only be obtained by sintering at or approaching 1700 ºC. Poor grain-boundary conductivities of zirconates severely keep them from the practical application. Several researches have shown that indium is able to enhance the chemical stability and sinterability of barium cerate and zirconate series proton conductors [42, 44, 61, 76]. Consequently, in the present work, indium was selected as a dopant to simultaneously maximize the chemical stability, sinterability and electrical conductivity of $BaCe_{0.8-x}Zr_xY_{0.2}O_{3-\delta}$.

3.2 Experimental section

Around 1.2 g of synthesized $BCZIY_x$ series powders were axially pressed into pellets (with a diameter of 1 inch and thickness of 1.2 mm). The green pellets were densified by sintering in air at 1450 °C for eight hours. The surface morphologies, grain size and microstructures of the sintered pellets were characterized by using a JEOL scanning electron microscope (SEM). The actual density of sintered pellets was determined based on geometrical measurements and a water immersion (Archimedes) method [56]. The theoretical density of the densified pellets was calculated from XRD data. For conductivity measurements, platinum paste electrodes were painted on both sides of the dense $BCZIY_x$ pellets and then fired at 950 °C for 30 min to remove the organic binders and form good bonding between the pellet and electrodes.

A conductivity test was assembled according to Figure 3.1. An AC impedance system consisting of a Solartron 1255 HF frequency response analyzer and a Solartron 1287 electrochemical interface was used to perform the conductivity test, with voltage intervals of 10 mV and frequency ranges from 0.1 Hz to 1 MHz. Electrochemical impedance spectra (EIS) were collected in different atmospheres and temperature range from 150 °C to 850 °C, controlled by a Thermolyne F79300 tubular furnace. The obtained EIS data were analyzed by the Zview modelling software.

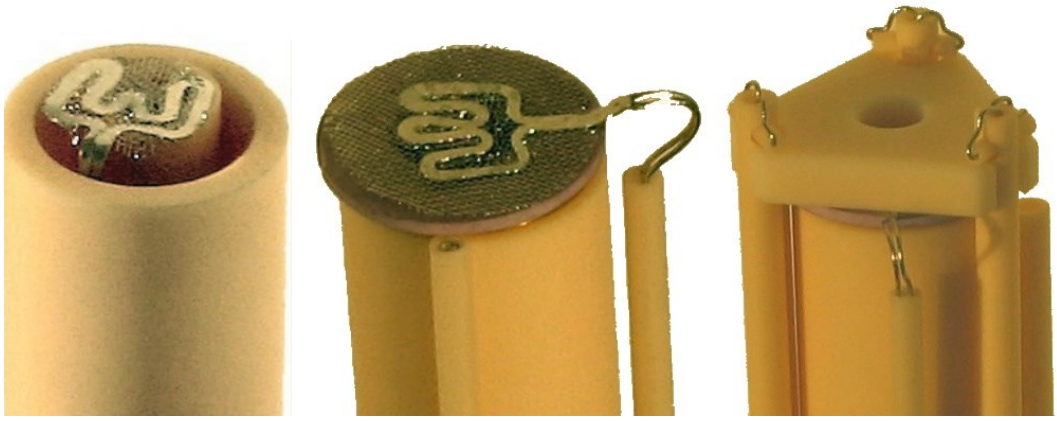

Figure 3.1 Schematic of conductivity test by the two-points method. Left: the bottom electrode pushed up by the inner gas supply tube. Middle: sample, thermocouple and top electrode. Right: spring load assembly pulling the setup tightly together.

3.3 Results and discussion

3.3.1 Sinterability test

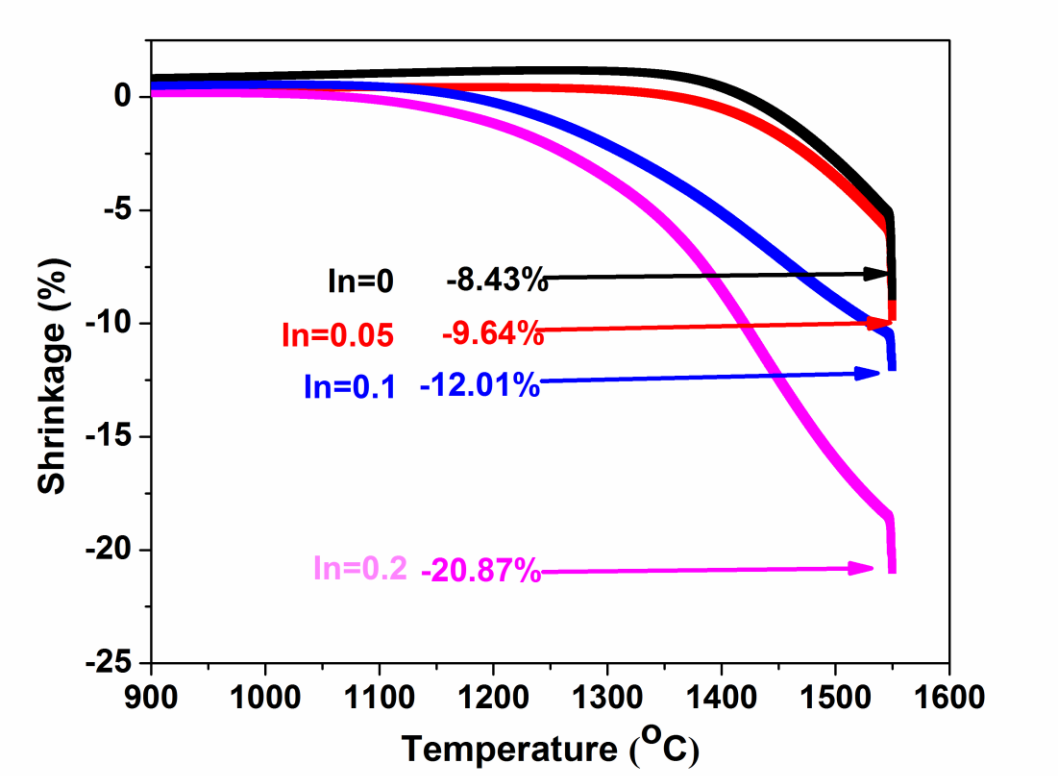

Figure 3.2 Shrinkage plots of $BCZIY_x$ (x=0, 0.05, 0.1, 0.2) samples.

Figure 3.2 describes the sintering behavior of $BCZIY_x$ samples with different In content. The temperature point at which $BCZIY_x$ with x=0.1 and 0.2 began to shrink was around 1122 °C, more than 200 °C lower than that for $BCZIY_x$ with x=0 and 0.05 (~1339 °C). After heating the sample up to 1550 °C at a rate of 10 °C/min and holding it for 30 min, the final shrinkage for the $BCZIY_x$ series aggravated when the In content was increased. The total shrinkage for the sample with In=0.2 was -20.87%, almost three times larger than that of sample

with In=0 (-8.43%). These shrinkage values of the $BCZIY_x$ samples appear to be comparable to those caused by other sintering methods reported in selected literature [63-65, 81].

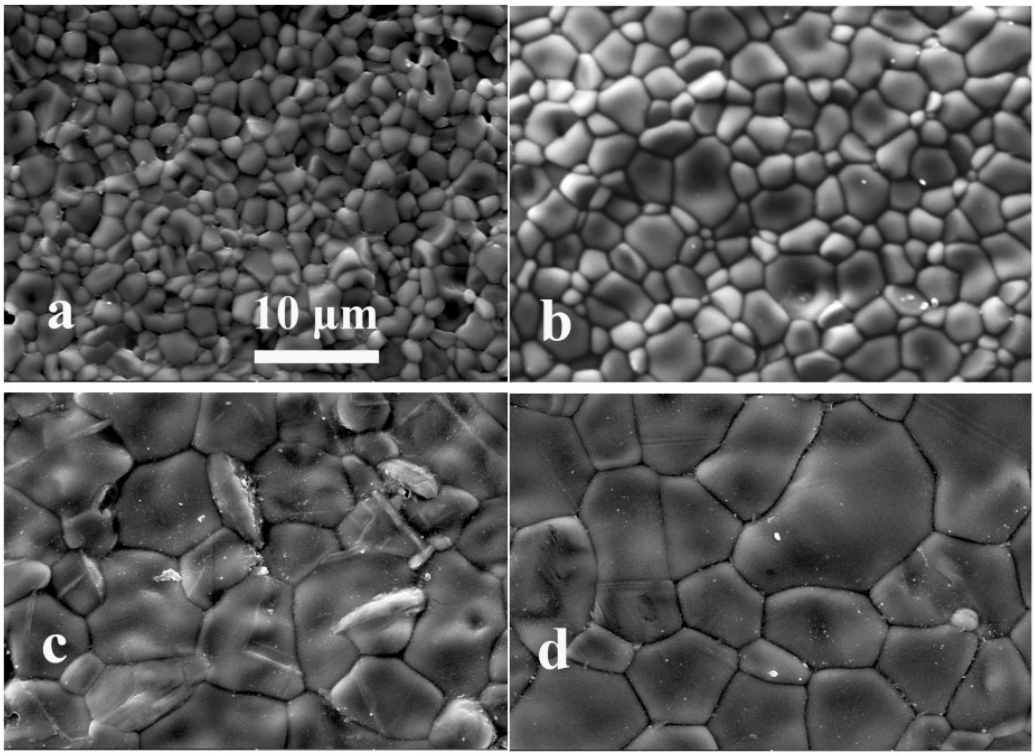

Figure 3.3 SEM images of dense $BCZIY_x$ (x=0, 0.05, 0.1, 0.2) pellets (a)x=0; (b)x=0.05; (c)x=0.1; (d)x=0.2.

Figure 3.3 shows the SEM images of surface morphologies of $BCZIY_x$ pellets densified by sintering in air at 1450 °C for 8 hours. All the sintered pellets exhibited quite low porosities (without connected holes or pores) and showed no visible indication of liquid phase formation or phase segregation at the grain boundary, which occurred in other proton conductor research [37].

As shown in the SEM images, the average grain size of densified pellets was apparently increased by In doping. The mean grain size for samples without

In doping was about 2 μm, in agreement with values in the references [50, 54]. For samples with In=0.1 and 0.2, the average grain size was almost 10 μm, remarkably larger than that of original $BaCe_{0.5}Zr_{0.3}Y_{0.2}O_{3-\delta}$ (BCZY) or other reported values obtained by sintering at an even higher temperature (e.g. 1600 °C) for a prolonged annealing time [45, 50, 53, 54]. A large average grain size can significantly reduce the overall grain boundary volume, which in turn helps to minimize the grain boundary resistance of proton conductors. This will be discussed in detail in the following section.

Table 3.1 Relative densities of densified $BCZIY_x$ series pellets sintered in air at different temperatures

In content	Relative density		
	1350 °C	1450 °C	1550 °C
0	73%	87%	92%
0.05	79%	92%	95%
0.1	86%	97%	99%
0.2	91%	98%	99%

Table 3.1 summarizes the relative densities of each $BCZIY_x$ sample sintered at 1350, 1450, and 1550 °C for 8 hours. Relative densities for each sample went up when the sintering temperature and the In doping content were increased. Specifically, at 1350 °C, only the sample with In=0.2 showed a relative density exceeding 90%, but when the sintering temperature rose to 1450 °C, indium-free BCZY remained as the only sample that still had a relative density of less than 90%, while the samples with In=0.1 and 0.2 both increased to higher than 97%.

When T=1550 ^{o}C, pellets of $BCZIY_x$ with x=0.1 and 0.2 reached nearly complete densification.

All the sinterability test results synergistically confirmed that In doping promoted the sintering activity of original BCZY. In may not be an ideal candidate as a sintering aid. However, its doping into BCZY could still be a promising strategy. Compared with other sintering aids, In is more preferable as a dopant when taking into account its simultaneous enhancement on chemical stability and tolerable adverse effect on the electrical conductivity [57, 63-65, 82].

3.3.2 Conductivity test

The ohmic resistance of a single cell is mainly determined by electrolyte resistance. Therefore, it is essential to investigate the electrical conductivity of $BCZIY_x$ to evaluate the feasibility of its being a potential proton conducting electrolyte material for SOFCs. EIS plots can be used to separate bulk and grain boundary contributions to the total resistance at a low temperature range (150-350 ^{o}C) [83, 84].

Figure 3.4 shows Nyquist plots of impedance spectra for $BCZIY_x$ (x=0, 0.05, 0.1, 0.2) in wet H_2 at 250 ^{o}C. All the plots consisted of three arcs at high, intermediate and low frequencies, corresponding to bulk, grain boundary and electrode resistance, respectively [40, 85]. However, rather than well-defined semicircles, distortion can be detected in all the separated arcs. This distortion has also been observed for other polycrystalline materials and is the consequence of the microstructure inhomogeneties of sintered pellets [83, 84]. For

$BaCe_{0.4}Zr_{0.3}In_{0.1}Y_{0.2}O_{3-\delta}$ ($BCZIY_{0.1}$), the non-uniform grain size distribution [Figure 3.3 (c)] could be the reason for the impedance spectra distortion.

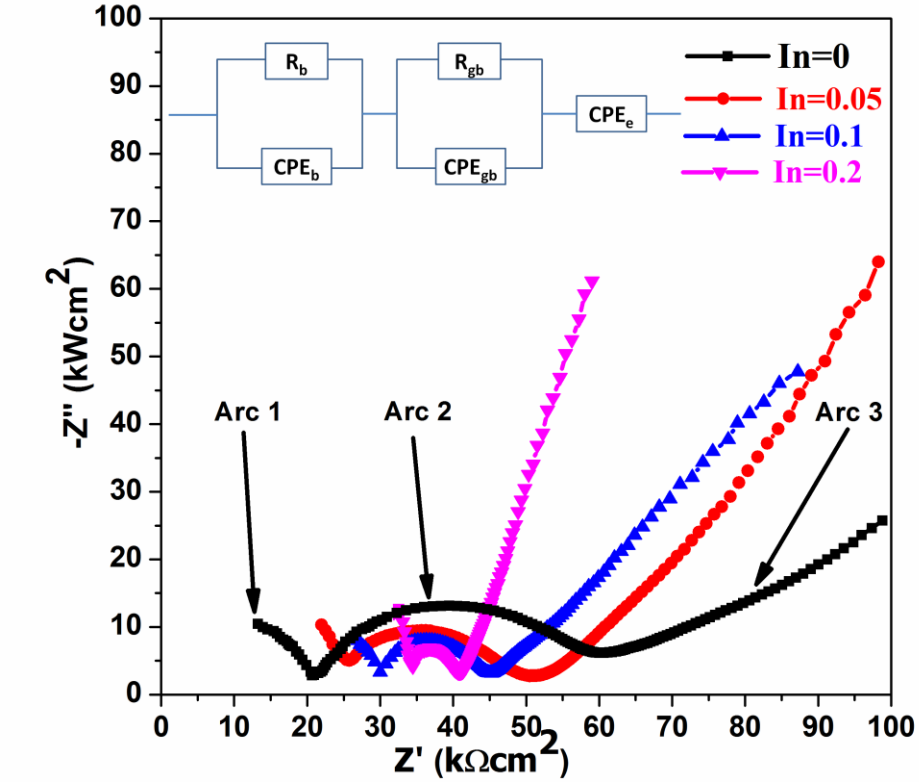

Figure 3.4 Impedance spectra of $BCZIY_x$ (x=0, 0.05, 0.1, 0.2) pellets at 250 °C in wet H_2 (H_2O 3 vol%).

To quantitatively evaluate the bulk and grain boundary resistance of each sample, an equivalent circuit $(R_bQ_b)(R_{gb}Q_{gb})Q_e$ (in Figure 3.4) was used to fit the Nyquist plot with Zview 2.0 Software. R and Q denoted the resistor and constant phase element (CPE) with b, gb, and e as the subscripts representing bulk, the grain boundary and the electrode process, respectively. The frequency corresponding to the first arc lay in the range of 700 KHz to 1 MHz, followed by

40 KHz to 100 KHz for the second arc. The capacitances for bulk and the grain boundary were calculated using the following equation [86]:

$$C = R^{\frac{1-n}{n}} Q^{\frac{1}{n}} \qquad (3.1),$$

where Q is a pre-exponential factor and n ($0 \leq n \leq 1$) is an exponent of the CPE. The fitting parameters and calculation results are summarized in Table 3.2. The capacitances calculated for the first and second arc are in the order of magnitude of 10^{-12} and 10^{-9} Fcm^{-1}, which typically refers to a property of bulk and the grain boundary process [40]. According to reference [78], the bulk and grain boundary conductivities were calculated using the equivalent circuit fitting parameter through the equation as below:

$$\sigma = \frac{L}{A}\frac{1}{R} \qquad (3.2),$$

where L is the pellet thickness and A is the transverse area. A summary of σ_b and σ_{gb} was given in Table 3.3. The temperature dependence of ionic conductivity can be described by an Arrhenius equation as the following form:

$$\sigma = \frac{\sigma_0}{T} e^{\frac{-E_a}{KT}} \qquad (3.3),$$

where σ_o is the pre-exponential factor depending on the concentration of charge carriers, the geometry of the crystal lattice and the frequency of lattice vibrations, while E_a is the activation energy describing energy barriers encountered by conducting ions, and k represents the Boltzman constant [36]. A linearized form of the Arrhenius equation $(Ln(\sigma T))=f(1000/T)$ can be used to extract the

activation energy and compare the conductivity values of examined samples in different atmospheres [36].

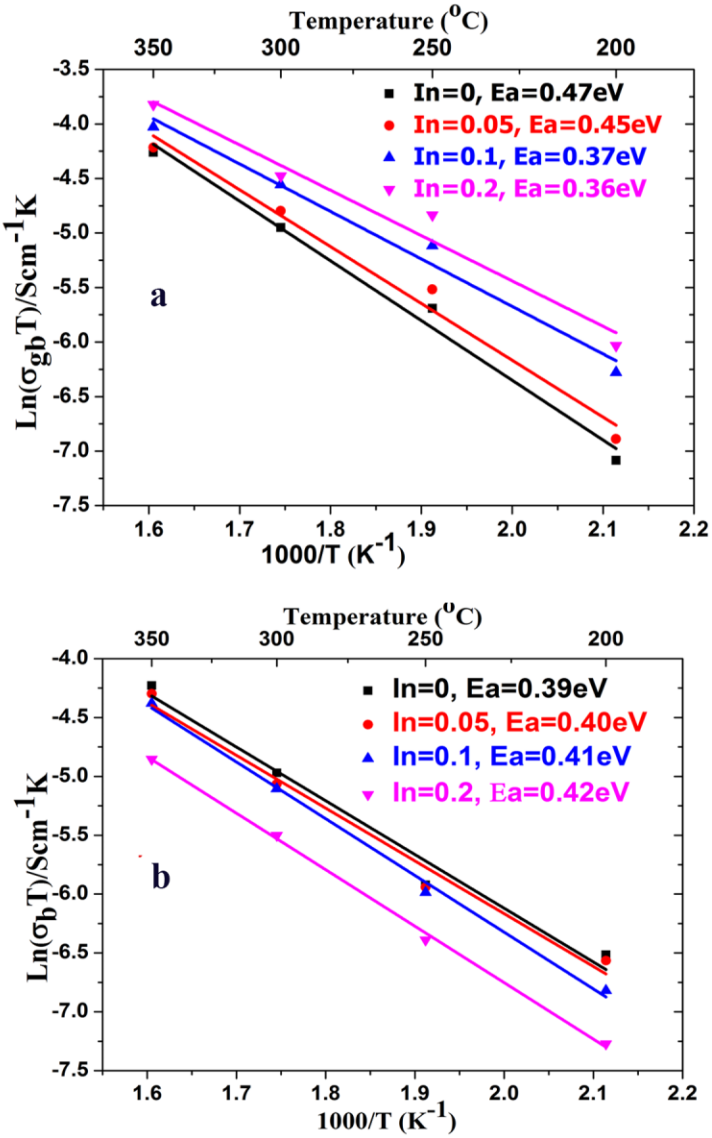

Figure 3.5 (a) Arrhenius plots of grain boundary conductivity and (b) bulk conductivity of $BCZIY_x$ (x=0, 0.05, 0.1, 0.2) pellets at 250 °C in wet H_2 (H_2O 3 vol%).

As shown in Figures 3.5 (a) and (b), the regression curves were obtained by a least squares linear fit. Figure 3.6 (a) shows the variations of activation energy corresponding to grain boundary conductivity and bulk conductivity with In

doping content. As can be seen in Table 3.3, there was no appreciable difference in the order of magnitude of σ_b and σ_{gb} for the different In doping content samples at the low temperature range (200-350 ºC) in wet H_2 (H_2O 3 vol%), and the values were comparable to that reported in references [36, 40]. Furthermore, Figure 3.5 (a) and (b) indicate that both the grain boundary conductivities and bulk conductivities increased with the rising temperature, facilitating the protons' mobility.

However, at a certain temperature point, e.g. 200 or 250 °C as shown in Figure 3.6 (b), σ_{gb} increased with increasing In doping content and σ_b exhibited a downtrend. Correspondingly, Figure 3.6 (a) indicates that energy barriers for protons transferring through the grain boundary went down with increasing In content, especially for samples with In concentrations from 0.05 (0.453 eV) to 0.1 (0.372 eV), covering a remarkable activation energy drop of 17.8%.

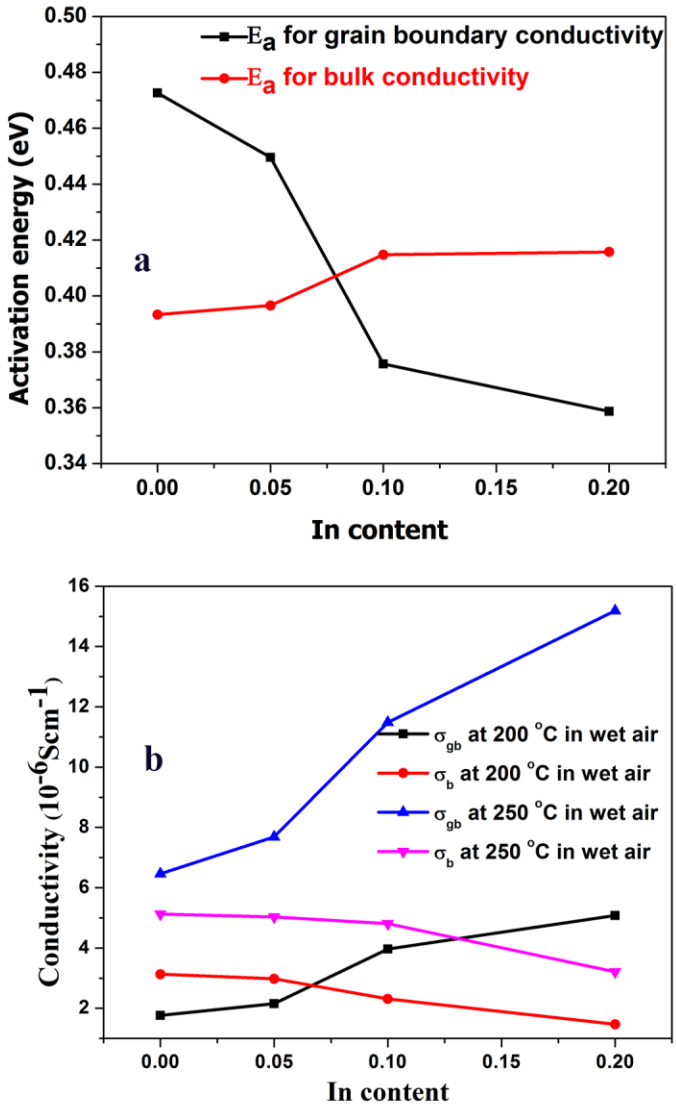

Figure 3.6 (a) Variation of the activation energy of grain boundary conductivity and bulk conductivity with In content. (b) Variation of the grain boundary conductivity and bulk conductivity of $BCZIY_x$ (x=0, 0.05, 0.1, 0.2) with In content at 200 °C and 250 °C in wet H_2 (H_2O 3 vol%).

In contrast, the activation energy of bulk conductivity increased slightly with the ascending In content. In other words, a higher In doping concentration favoured grain boundary conductivity, which could be ascribed to the decreasing grain boundary volume resulted from the increasing average grain size and rising

relative density at the higher In doping level. This is in agreement with the results from the sinterability test. Moreover, the bulk conductivity appeared to be negatively affected by the larger In doping, in spite of the induced and more favourable tolerance factors. The underlying reason for this could be that the basicity of the O-H bond was likely modified by the addition of In, because the parent lattice structure adjacent to the In sites was reorganized [11, 87].

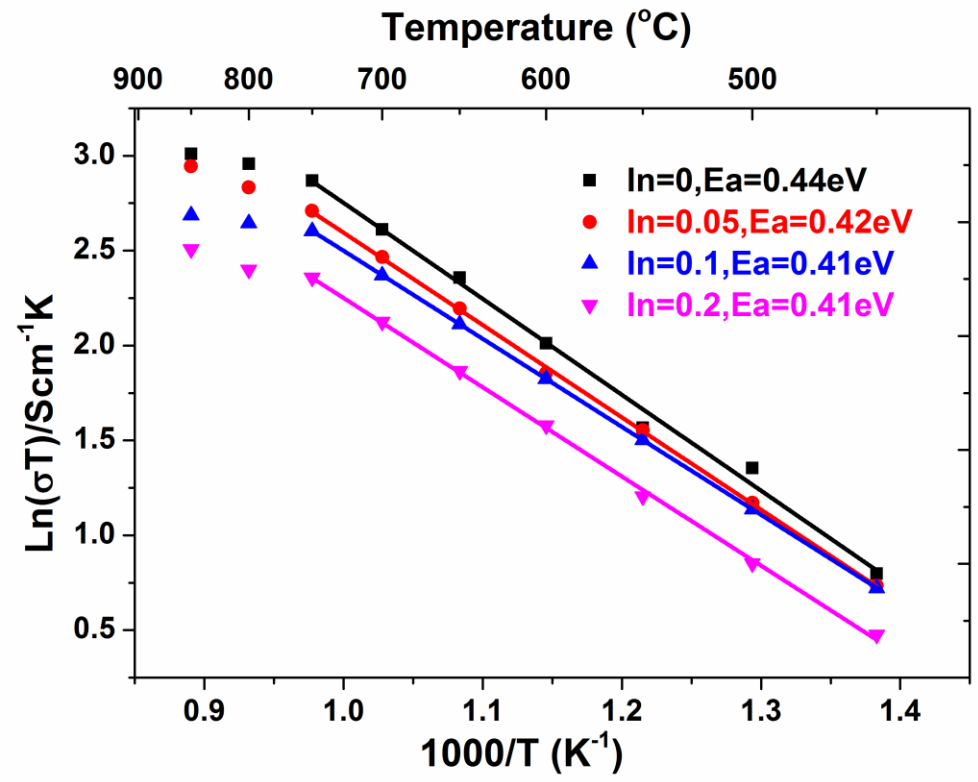

Figure 3.7 Arrhenius plots of total conductivity of $BCZIY_x$ (x=0, 0.05, 0.1, 0.2) pellets in wet (3 vol% H_2O) H_2.

At a high temperature range of 450-850 °C, arcs representing bulk and grain boundary resistances were not visibly separated in the EIS spectra and the overall conductivity was mainly determined by bulk conductivity [37]. Figure 3.7 shows Arrhenius plots of total conductivity for the $BCZIY_x$ series in a humid H_2

atmosphere. It is clear that all the $BCZIY_x$ compositions shared a similar trend of the conductivity varying with testing temperatures. Specifically, in the temperature range of 450 °C to 750 °C, the total conductivity demonstrated a rising trend with an increase in temperature. However, at temperatures ≥ 800 °C, the rising trend of total conductivity was restrained by the higher temperature, as indicated by the flatter portion of the curves at the T≥ 800 °C region.

In a dry H_2 atmosphere, hydroxide defects are mainly formed via the following reaction:

$$H_2 + 2O_O^{\times} \leftrightarrow 2(OH)_O^{\bullet} + 2e' \quad (3.4)$$

However, the most important reaction generating the protonic defects is considered to be the dissociative adsorption of water [11], which can be expressed by the Kröger-Vink notation as shown below:

$$H_2O + V_O^{\bullet\bullet} + O_O^{\times} \leftrightarrow 2(OH)_O^{\bullet} \quad (3.5)$$

In this reaction, water from the gas phase dissociates into a hydroxide ion and a proton; the former fills an oxygen vacancy while the latter can form a covalent bond with lattice oxygen [11, 43]. Water adsorption [shown as eq. 3.5] consumes oxygen vacancies and is exothermic and thus, can be suppressed by a higher temperature. Thermodynamically, a higher temperature benefits the mobility of proton defects, leading to lower activation energy of proton conduction indicated by a reduced slope of Arrhenius plots in Figure 3.7. Nevertheless, the proton conductivity dropped due to the decreased concentration of proton defects, caused by supressed hydration process of perovskites in high

temperature range. In addition, in this reducing atmosphere, proton conduction is predominant while the oxygen ions' conduction is limited and the electronic conduction is almost negligible. This accounts for the slight slope drop of Arrhenius plots of total conductivity of the $BCZIY_x$ series in a humid H_2 atmosphere.

It is also worth noting that in Figure 3.7, a higher In doping level induces the decrease of total conductivity in the 450 – 850 °C temperature range, and the activation energy of proton conduction showed a slight descent with an increase in the In doping amount (similar to the grain boundary conductivity in the low temperature range). Activation energies of ionic conduction are determined by the type of charge carriers, microstructure of the host matrix, and chemical and electronic properties of the surrounding ions [11, 83, 84]. A smaller grain boundary volume and better uniformity of the grain interior resulting from a larger grain size caused by higher In doping may partially account for the downtrend in activation energies of total conductivity. Proton conductivity is thought to be mainly determined by the concentration and mobility of proton defects. Equation 3.5 indicates that the proton defects' concentration is proportional to the amount of oxygen vacancies formed by incorporating a lower valence (usually +3) dopant. However, a higher In doping level does not necessarily result in a large proton defect concentration. The reason is that the water solubility limit was found to approach the dopant concentration only for perovskite oxide with a tolerance factor close to unity [11]. Furthermore, as shown in Table 2.2, the absolute value of tolerance factors of $BCZIY_x$ compounds

was far from unity, and the optimization of the tolerance factor induced by In doping was quite limited. In addition, Giannici et al. [11, 87] stated that In doping likely modifies the basicity of the O-H bond since a structural reorganization of the host matrix around the In-doped sites occurs, as discussed above. Therefore, the large In doping amount may additionally impair the proton defects' mobility. Overall, In doping still largely obeys the widely accepted trade-off relationship between chemical stability and proton conductivity for most proton conductors.

Table 3.4 compares the conductivities of samples from the present work with representative references in similar test conditions. Orders of magnitude of total conductivities for the $BCZIY_x$ series in this work were 10^{-2} and 10^{-3}. At 700 ^{o}C, overall conductivities showed a downtrend as the In content increased. This is the same trend as at 650 and 600 ^{o}C. Specifically, for In=0.1 at 700 ^{o}C, BCZIY offered a conductivity of 1.1×10^{-2} Scm^{-1} in humid H_2, which was fairly comparable to other proton conductors reported by selected references. The difference in electrical properties between the samples in this work and the materials in the cited literature was probably due to the difference in compositions and process routes. With a comprehensive approach to considering the chemical stability, sinterability and electrical conductivity, $BaCe_{0.4}Zr_{0.3}In_{0.1}Y_{0.2}O_{3-\delta}$ was chosen as the optimal composition in the subsequent sections.

Figure 3.8 shows temperature dependence of total conductivity of $BaCe_{0.4}Zr_{0.3}In_{0.1}Y_{0.2}O_{3-\delta}$ in different atmospheres. Obviously, the wet conditions always provided larger conductivities than dry conditions when the whole

temperature range was tested, confirming that $BaCe_{0.4}Zr_{0.3}In_{0.1}Y_{0.2}O_{3-\delta}$ exhibited proton conductivity.

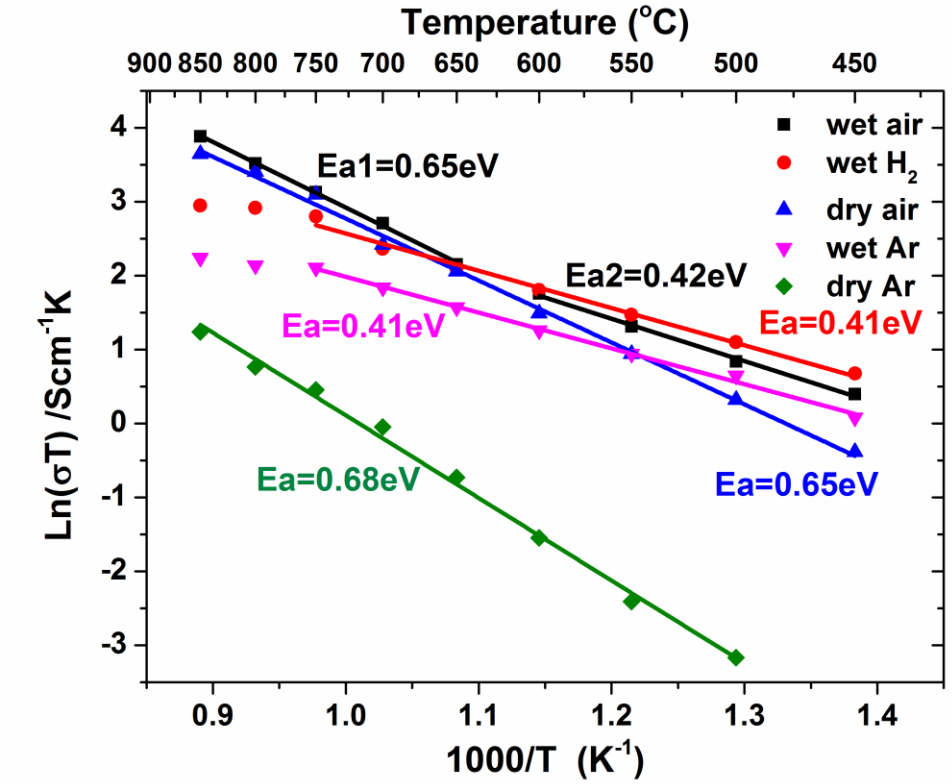

Figure 3.8 Arrhenius plot of total conductivity of $BaCe_{0.4}Zr_{0.3}In_{0.1}Y_{0.2}O_{3-\delta}$ pellets tested in different atmospheres.

When T < 650 °C, wet H_2 was the most favourable atmosphere for electrical conductivity, closely followed by wet air, whereas at T > 700 °C, wet air provided the highest conductivity, with dry air taking a close second place. Furthermore, the uptrend of conductivity in wet H_2 was apparently weakened in the higher temperature range (750 °C < T <850 °C). Across the temperature range tested, dry argon appeared as the most adverse atmosphere for the total conductivity of $BaCe_{0.4}Zr_{0.3}In_{0.1}Y_{0.2}O_{3-\delta}$. The activation energies corresponding to

wet H_2 and wet argon were both around 0.4 eV, consistent with the values reported by references [36, 38, 55, 88].

Dry argon held the highest activation energy of 0.68 eV compared with the other atmospheres. For wet air, there were two different situations: first, when T ≤ 600 ºC, the activation energy was 0.42 eV, almost the same as with wet H_2 and wet argon; and second, when T ≥ 650 ºC, it increased to 0.63 eV, nearly equal to that in dry air (0.65 eV). These characteristics of the conductivities observed in different atmospheres should be attributed to the changes in charge carriers, caused by the factors such as H_2O partial pressure, oxygen partial pressure and testing temperatures [4, 11, 43]. Protons, oxygen ions and electron holes are considered the three main sources for the overall conductivity of proton conductors [11]. The formation and conduction of protons have been discussed in previous sections. Since oxygen ions are intrinsic in perovskite oxides, the generation of electron holes can be facilitated by oxidizing conditions, as illustrated by the following reaction:

$$O_2 + 2V_O^{\bullet\bullet} \leftrightarrow 2O_O^{\times} + 4h^{\bullet} \tag{3.6}$$

In the lower temperature range (450 °C ≤ T ≤ 650 ºC) and wet atmospheres, protons are the predominant charge carriers due to their low activation energy. In this case, for the same co mpound, proton conductivity is mainly determined by proton concentration, which is most preferable in a pure and wet H_2 atmosphere. However, the progressive increase in temperature (T ≥ 700 ºC) supresses the hydration reaction of perovskite oxide, which competes with the electron holes' formation reaction for oxygen vacancies. As a consequence, the electron-holes

and oxygen ions will proportionally make more contributions to the total conductivity in a higher temperature range and under higher oxygen partial pressure. As for dry argon, the only available sources for electrical conductivity are intrinsic oxygen ions, which have to overcome a higher activation energy barrier (0.65 eV) than protons for conduction.

Table 3.2 Fitting parameters of impedance plots obtained with $BCZIY_x$ samples at 250 °C in wet H_2 (H_2O 3 vol%)

In content	Fitting parameters							
	Bulk				Grain boundary			
	R ($10^4\Omega$)	Q ($10^{-11}F.cm^{-1}$)	n	C ($10^{-12}F.cm^{-1}$)	R ($10^4\Omega$)	Q ($10^{-8}F.cm^{-1}$)	n	C ($10^{-9}F.cm^{-1}$)
0	1.99	2.5	0.87	1.6	8.87	1.4	0.82	5.18
0.05	2.03	3.1	0.85	1.9	6.71	3.2	0.81	4.21
0.1	2.12	1.9	0.91	1.38	1.58	2.8	0.78	2.69
0.2	3.17	2.9	0.92	2.36	1.33	2.5	0.83	2.21

Table 3.3 Grain boundary and bulk conductivities of $BCZIY_x$ samples at a low temperature range in wet H_2 (H_2O 3 vol%)

In content	Conductivity ($10^{-6}Scm^{-1}$)							
	200 °C		250 °C		300 °C		350 °C	
	σ_{gb}	σ_b	σ_{gb}	σ_b	σ_{gb}	σ_b	σ_{gb}	σ_b
0	1.77	3.13	6.46	5.13	12.36	12.12	22.64	23.41
0.05	2.15	2.98	7.68	5.03	14.4	11.01	23.7	21.82
0.1	3.97	2.31	11.48	4.81	18.31	10.59	28.59	20.12
0.2	5.08	1.47	15.19	3.21	19.85	7.12	35.12	12.52

Table 3.4 Conductivities of the $BCZIY_x$ samples in the present work and those reported by representative references. All samples were tested in humid wet H_2 (containing H_2O 3 vol%)

Samples	Conductivity (Scm^{-1})			Activation energy (eV)	Published year
	600 °C	650 °C	700 °C		
$BaCe_{0.5}Zr_{0.3}Y_{0.2}O_{3-\delta}$	8.5×10^{-3}	1.1×10^{-2}	1.3×10^{-2}	0.44	present work
$BaCe_{0.45}Zr_{0.3}In_{0.05}Y_{0.2}O_{3-\delta}$	7.6×10^{-3}	9.7×10^{-3}	1.2×10^{-2}	0.42	
$BaCe_{0.4}Zr_{0.3}In_{0.1}Y_{0.2}O_{3-\delta}$	7.1×10^{-3}	8.9×10^{-3}	1.1×10^{-2}	0.41	
$BaCe_{0.3}Zr_{0.3}In_{0.2}Y_{0.2}O_{3-\delta}$	5.5×10^{-3}	7.0×10^{-3}	8.6×10^{-3}	0.41	
1-$BaCe_{0.7}Ta_{0.1}In_{0.2}O_{3-\delta}$	0.87×10^{-3}	1.35×10^{-3}	----	----	2013
$BaCe_{0.75}Zr_{0.1}Sm_{0.15}O_{3-\delta}$ [33]	----	----	1.3×10^{-2}	0.33	2013
$BaCe_{0.55}Zr_{0.3}Sm_{0.15}O_{3-\delta}$ [33]	----	----	1.0×10^{-2}	0.44	2013
$BaZr_{0.8}In_{0.2}O_{3-\delta}$ [38]	----	----	1.0×10^{-3}	0.5	2013
$BaCe_{0.5}Zr_{0.3}Gd_{0.15}Pr_{0.05}O_{3-\delta}$ [37]	----	----	7.6×10^{-3}	0.71	2013
$BaCe_{0.65}In_{0.3}Ti_{0.05}O_{3-\delta}$ [17]	----	----	5.0×10^{-3}(750 °C)	0.45	2013
$BaCe_{0.7}Zr_{0.1}Y_{0.1}Yb_{0.1}O_{3-\delta}$ [18]	----	----	7.4×10^{-2}(750 °C)	0.45	2013
$BaCe_{0.7}Y_{0.2}Pr_{0.1}O_{3-\delta}$ [42]	----	----	1.21×10^{-2}	----	2013
$Ba_{0.8}Sr_{0.2}Ce_{0.6}Zr_{0.2}Y_{0.2}O_{3-\delta}$ [22]	----	----	9×10^{-3} (800 °C)		2012
$BaCe_{0.7}In_{0.2}Yb_{0.1}O_{3-\delta}$ [24]	2.7×10^{-3}	----	4.5×10^{-3}(800 °C)	0.25	2011
$BaCe_{0.6}Zr_{0.3}Y_{0.1}O_{3-\delta}$ [7]	----	----	1×10^{-2}	0.35	2000
$BaZr_{0.7}Pr_{0.1}Y_{0.2}O_{3-\delta}$ [15]	----	----	----	0.51	2010
$BaCe_{0.7}Zr_{0.1}Y_{0.1}Yb_{0.1}O_{3-\delta}$ [36]	----	----	5×10^{-2}	----	2009
$BaCe_{0.5}Zr_{0.3}Y_{0.2}O_{3-\delta}$ [9]	----	----	1.14×10^{-2}	0.41	2008

Chapter 4 Fabrication and characterization of anode support fuel cell

4.1 Introduction

To minimize the ohmmic resistance, researchers need to develop novel materials having improved electrical conductivity, to reduce the thickness of electrolyte or to use a combination of both strategies. In recent years, both electrolyte-supported and electrode-supported SOFCs with different materials have been intensively investigated. In electrolyte-supported cells, the thickness of the electrolyte typically ranges from 50to150 μm, leading to a high ohmic resistance. In contrast, in electrode-supported designs, the thickness of the electrolyte can be much thinner, typically in the range of 5-20 μm, which reduces the ohmic resistance and makes the designs more suitable for intermediate temperature operation (500-700 ^{o}C) [89].

4.2 Experimental section

Given the comprehensive consideration of the chemical stability, sinterability and electrical conductivity, the $BaCe_{0.4}Zr_{0.3}In_{0.1}O_{3-\delta}$ ($BCZIY_{0.1}$) sample was selected as the electrolyte material. The anode-supported PC-SOFCs were fabricated using a spin-coating method: $BCZIY_{0.1}$, NiO and starch (working as pore formers) with a weight ratio of 60:40:20 were uniformly mixed in a blender with a rotating speed of 80 rpm for 12 hours. Subsequently, ~1.2 g of the resulting mixed powders was axially pressed into discs (with diameter of 1 inch and thickness of 2 mm) at 200 MPa for 1 min. To remove the organic pore

formers and ensure appropriate mechanical strength, the obtained green anode support pellets were calcined at 1150 °C for 2 hours.

Table 4.1 Recipe of organic vehicle for spin coating

	Chemicals	**Information**	**Content (wt%)**
Binder	B76-PVB	Talas	5
Solvent	Isopropanol	Fisher, 99.9%	71
	α-Terpineol	Alfa Aesar, 96%	20
	Triethanolamine	Sigma-Aldrich, 99.9%	2
	Poly(ethylene glycol) 400	Aldrich	2

$BCZIY_{0.1}$ electrolyte thin film was deposited onto the anode substrate with a spin coating method. The flat substrates polished with sandpaper were fixed on a spin coating plate (Cookson Electronics Equipment, specially coating system). A thin film of stable suspension was spin coated onto the substrates at a high spinning rate of 3450 rpm for 25 s and then dried, followed by evaporating and burning out part of solvent with a heater. The thickness of the membrane was controlled by the cycles of spinning coating. The stable $BCZIY_{0.1}$ slurry used for spin coating was a mixture of 20 wt% $BCZIY_{0.1}$ and 80 wt% organic vehicle,

obtained by ultrasound-mixing for 30 min. The recipe of the organic vehicle is given in table 4.1.

At this time, porous anode substrate with wet $BCZIY_{0.1}$ electrolyte film was co-sintered at 1400 °C for 5 hours to densify the thin film electrolyte. 1400 °C was used because an extremely high sintering temperature favors the densification of electrolytes but undermines anode porosity. Finally, a composite cathode material consisting of equal amounts of $BCZIY_{0.1}$ and $Ba_{0.5}Pr_{0.5}CoO_{3-\delta}$ (BPC) was pasted onto the densified electrolyte via screen printing and sintered at 950 °C for 1 hour to obtain the final membrane electrode assemblies (MEA). The resulting active area of the cathode was 0.5 cm^2.

As shown in Figure 4.1, to test the cell performance, the obtained anode support fuel cell was fed by humid pure H_2 (containing 3 vol% of H_2O) at the anode side and static air at the cathode side, operated at temperatures ranging from 600 to 750 °C at incremental interval of 50 °C, controlled by a Thermolyne F79300 tubular furnace. The flow rate of the fuel gas was maintained at 25 mL/min. The anode side was sealed with Au paste. Two gold wires were connected to each of the electrodes as current collectors. The cell performance test was performed by the same EIS equipment with a conductivity measurement. After the electrochemical test, the configuration and microstructure of the anode support fuel cell were characterized by a JEOL SEM.

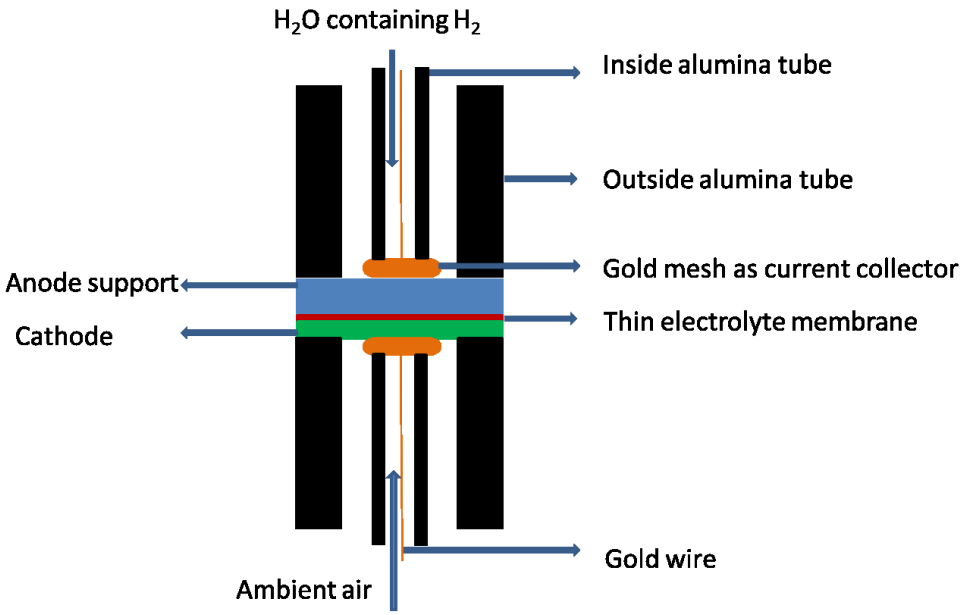

Figure 4.1 Schematic of anode support fuel cell testing method

4.3 Results and discussion

Conventional electrolyte-supported PC-SOFCs rarely provide maximum power density higher than hundreds of mW/cm^2, partially due to the large ohmic resistance caused by thick electrolytes [4, 58]. Reducing the thickness of the electrolyte down to a micrometer scale has been proven to be an efficient way to decrease the ohmic resistance and improve the cell performance. Electrode-supported fuel cells, on the other hand, allow the electrolyte thickness to be ~10 μm, but they require excellent sintering activity of electrolyte materials to ensure the adequate porosity of supporting electrodes when sintered at higher temperatures. After considering the overall chemical stability, sinterability and electrical conductivity, BCZIY0.1 was selected as the proton conductive electrolyte material to fabricate anode support fuel cells, with nickel and BPC as anode and cathode catalysts, respectively.

Figure 4.2 describes the I-V curve and power density plot at different temperatures for the single cell: Ni/BCZIY$_{0.1}$/BPC fed by humid H_2 (containing 3 vol% of H_2O) at the anode side and static air at the cathode side. The open circuit voltage (OCV) slightly decreased when the operating temperature was increased. The OCV had values of 1.05, 1.03 and 0.98 V at 600, 650 and 700 ºC, respectively. These values were close to those reported in previous studies [55-57, 90], indicating that adequate densification of the BCZIY$_{0.1}$ electrolyte can be achieved by sintering under relatively mild conditions (1400 °C for 5 hours).

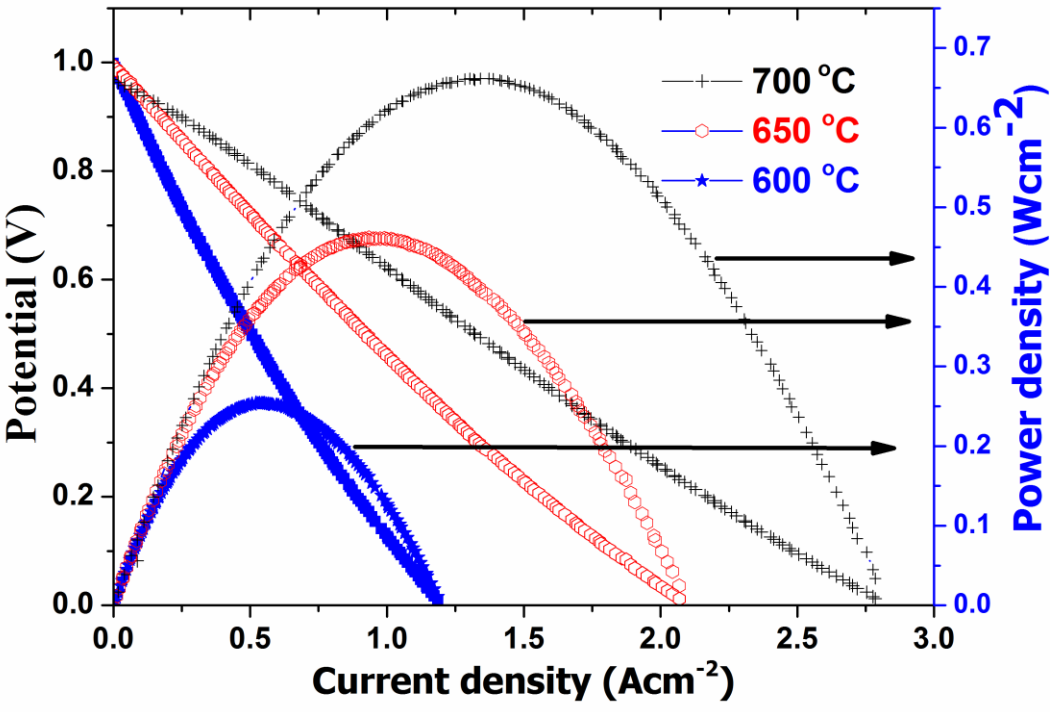

Figure 4.2 IV plots and power densities varying with current density

This also confirmed the improved sinterability of the electrolyte. The maximum power densities were found to rise when the testing temperatures

increased, with 253, 456 and 651 mW/cm^2 corresponding to 600, 650 and 700 ^{o}C, respectively.

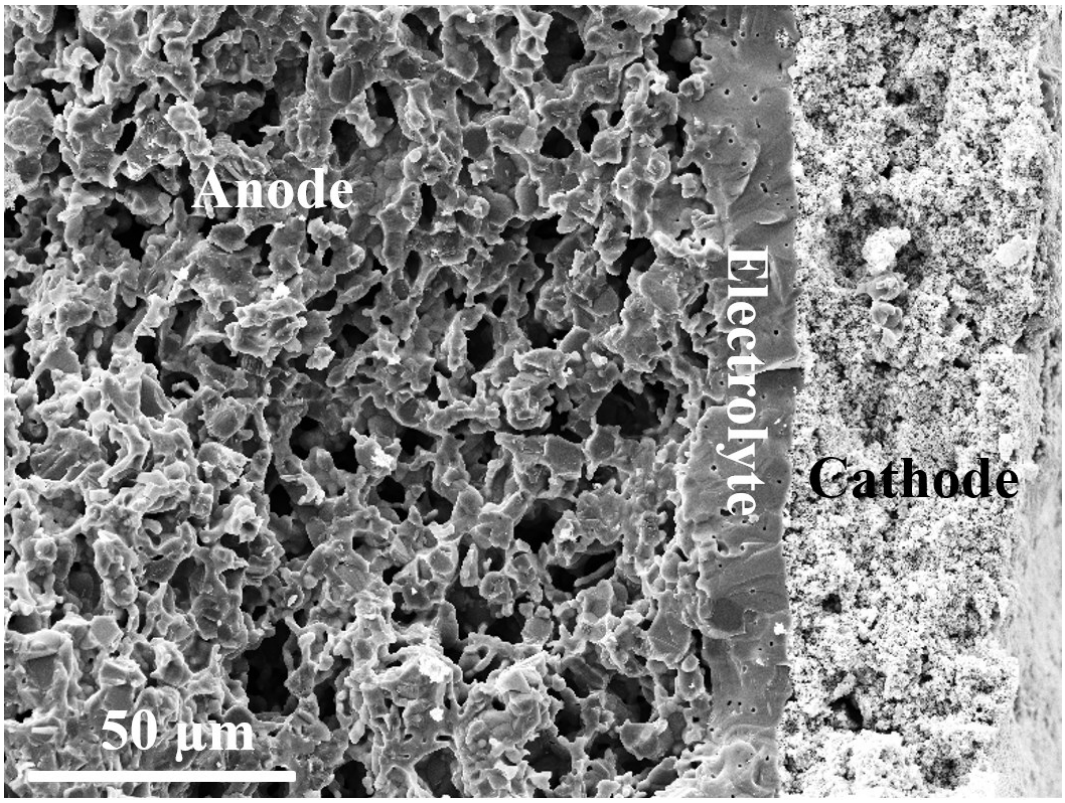

Figure 4.3 SEM image of configuration of the anode support fuel cell with $BaCe_{0.4}Zr_{0.3}In_{0.1}Y_{0.2}O_{3-\delta}$ as the electrolyte

Figure 4.3 shows the SEM micrographs of the configuration of the single anode-supported fuel cell after the stability test with $BCZIY_{0.1}$ as the electrolyte material. The electrodes kept a high porosity with an average hole diameter of 10 µm for anodes. The electrolyte was well densified and was about 15 µm thick without any connected pin holes or cracks, which validated the obtained OCV values and the results of the sinterability test. The $BCZIY_{0.1}$ electrolyte was ideally bonded with the anode and cathode layers.

The anode support fuel cell with the present $BCZIY_{0.1}$ as an electrolyte generated a maximum power density of 651 mW/cm^2 at 700 °C when fed by humid H_2. This value is comparable to or even better than the results reported by the representative references [55-57, 90].

Figure 4.4 shows the stability of the present fuel cell at 650 °C fed by humid H_2. The OCV value and the maximum power density did not drop from 1.03 V and 451 $mWcm^{-2}$ during the 100-hour test, indicating the adequate stability of the electrolyte in a humid atmosphere.

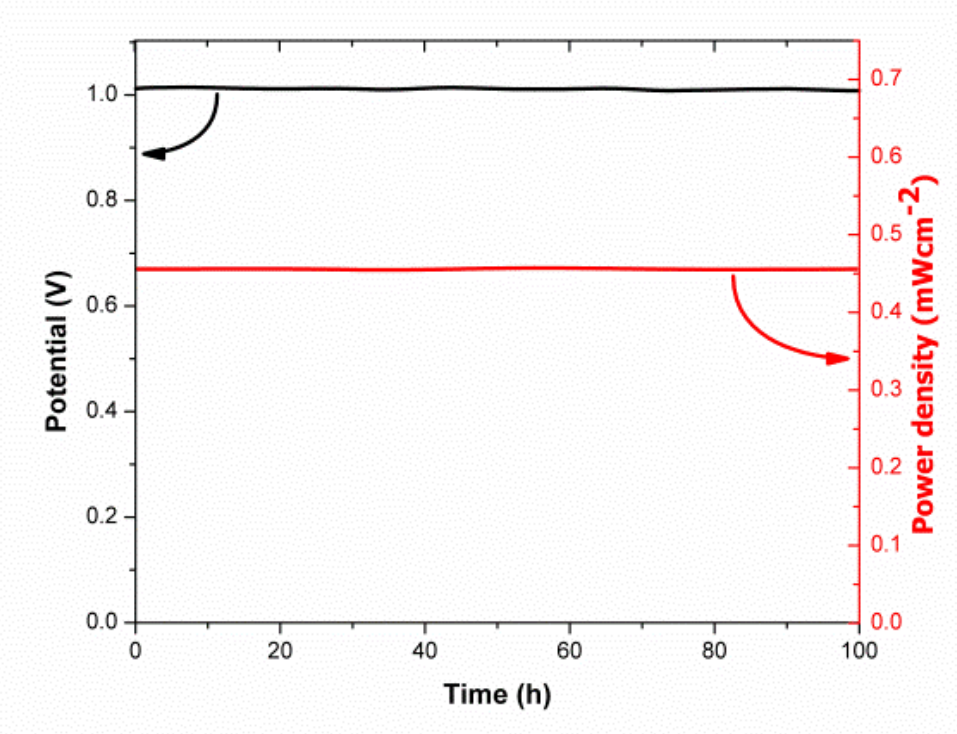

Figure 4.4 Stability test result in humid H_2 atmosphere and at 650 ºC

Regardless of the external operating parameters, the final cell performance was significantly dependent on the internal factors (e.g., type and compositions of selected materials and cell configuration) and the material process route [11, 56,

90]. The good cell performance achieved in the present work is an accumulative reflection of multiple contributing factors such as the high porosity of electrodes, good bonding and the connection between the electrodes and electrolytes, excellent densification and the relatively high electrical conductivity of electrolytes.

To further reduce ohmic resistance, a more uniform and thinner electrolyte membrane can be fabricated by novel technologies, such as pulsed laser deposition (PLD) [74] or atomic layer deposition (ALD) [73] . However, at the present stage, PLD and ALD seem to be suitable only for small scale application. Part of the reason is their much higher operating cost.

Fuel cell performance can be affected not only by the property and geometric dimension of electrolytes but also by the electrode polarization which considerably decreases when the operating temperature is increased [58, 90]. Similar to the conductivity test, resistances for the electrolytes and electrodes were investigated by the EIS measurement.

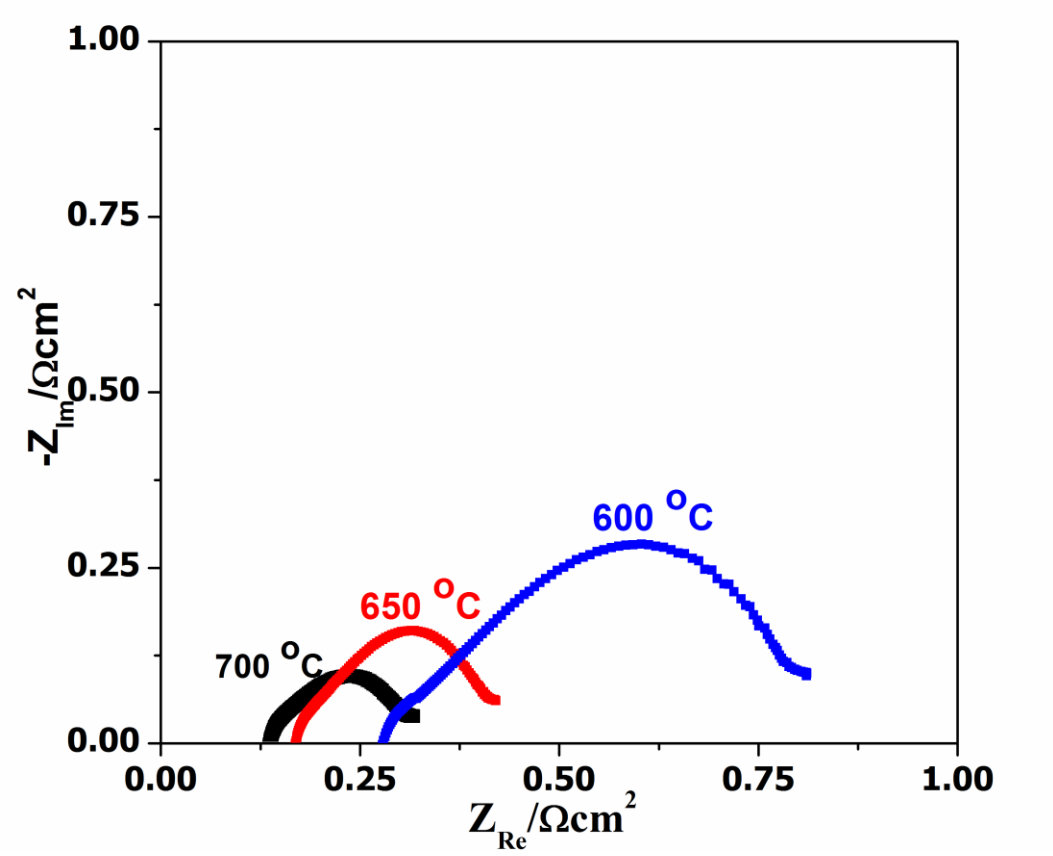

Figure 4.5 Impedance plots of $BCZIY_{0.1}$ at different operating temperatures in wet H_2

The intercepts corresponding to the low frequency section were obtained by fitting the plots with a (RQ) equivalent circuit. Consequently, the total interfacial polarization resistance can be calculated as the difference between the high frequency and low frequency intercepts [56]. Figure 4.5 shows the Nyquist plots in a complex plane of the present fuel cell test in humid H_2 at 600, 650, and 700 ^oC, respectively. The intercepts of plots with the real axis at high frequency sections represented the ohmic resistance (R_Ω), which resulted from electrolyte resistance and lead wires [58].

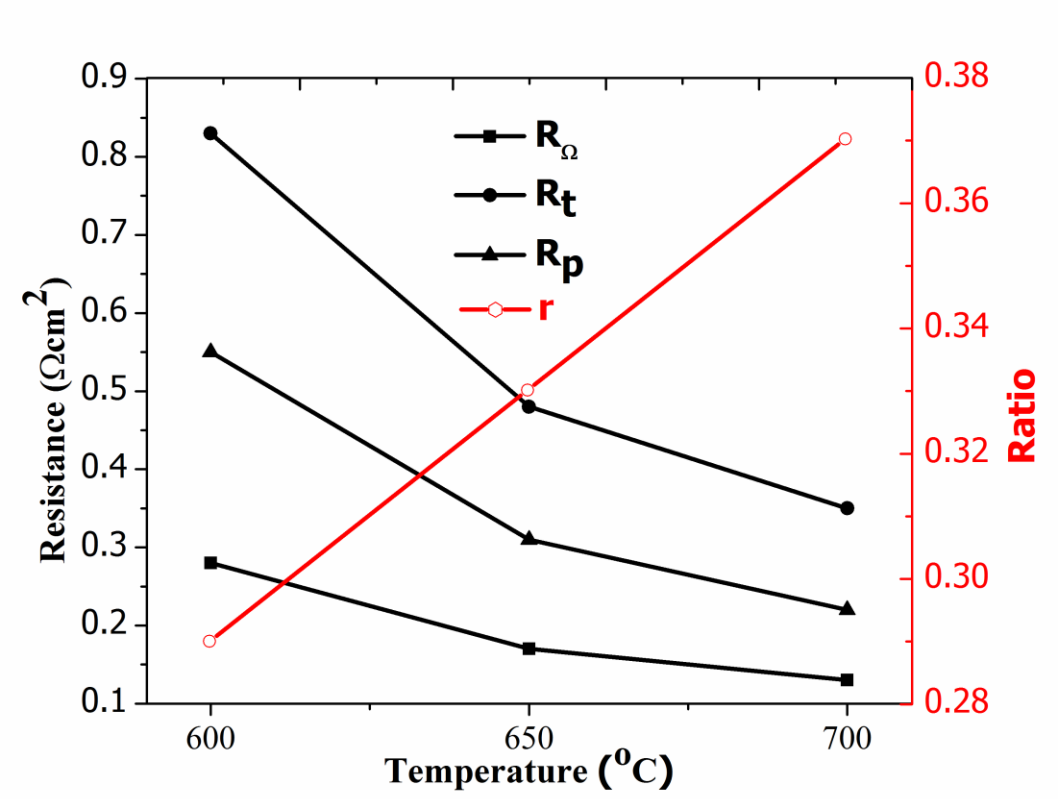

Figure 4.6 Variation of ohmic resistance (R_Ω), polarization resistance (R_p), total resistance (R_t), and the ratio (r) of R_Ω to R_t with testing temperature

Figure 4.6 illustrates the temperature dependence of ohmic resistance (R_Ω), polarization resistance (R_p), total resistance (R_t) and the ratio (r) of R_Ω to R_t. The R_Ω values corresponding to 600, 650 and 700 °C were 0.28, 0.17 and 0.13 Ωcm^2, respectively, and the R_t at 600, 650 and 700 °C were 0.83, 0.48 and 0.35Ωcm^2, respectively. The ratio increased with the testing temperature from 29.5% (600 °C) to 37.0% (700 °C). This suggested that ohmic resistance made an increasing contribution to the total resistance. However, the contribution from ohmic resistance was still less than the polarization resistance. Additionally, the ohmic resistance of the fuel cell appeared to be relatively smaller than the generally

reported values [55-57, 90], which could be partially ascribed to the improved sinterability and good conductivity of the electrolyte.

In the present work, in order to more effectively evaluate the properties of the $BCZIY_x$ electrolyte and the cell performance, the anode support fuel cell was fed by humid pure H_2. However, future research should focus more on using hydrocarbon gases as the fuel, as they are much more cost effective. Moreover, much work needs to be done on discovering the appropriate electrode materials that exhibit better compatibility with this novel electrolyte and can efficiently suppress carbon deposition and tolerate sulfur poisoning.

Chapter 5 Conclusions and future work

Effect of indium doping on the chemical stability, sinterability and electrical properties of original $BaCe_{0.5}Zr_{0.3}Y_{0.2}O_{3-\delta}$ was systematically investigated. The results showed that indium doping can significantly enhance the chemical stability and sinterability of $BaCe_{0.5}Zr_{0.3}Y_{0.2}O_{3-\delta}$. However, total conductivity of $BaCe_{0.5}Zr_{0.3}Y_{0.2}O_{3-\delta}$ in humid H_2 slightly reduced when indium concentration increased. $BaCe_{0.4}Zr_{0.3}In_{0.1}Y_{0.2}O_{3-\delta}$ has been proven to be the optimal composition which simultaneously maximized the chemical stability, sinterability and electrical conductivity. The electrical conductivity of $BaCe_{0.4}Zr_{0.3}In_{0.1}Y_{0.2}O_{3-\delta}$ reached 1.1×10^{-2} Scm^{-1} in wet hydrogen at 700 °C compared with the 1.3×10^{-2} Scm^{-1} for original $BaCe_{0.5}Zr_{0.3}Y_{0.2}O_{3-\delta}$. Anode support fuel cell with a thin $BaCe_{0.4}Zr_{0.3}In_{0.1}Y_{0.2}O_{3-\delta}$ electrolyte (15 μm) was fabricated by spin coating method. Maximum power density of 651 mW/cm^2 was obtained when operating at 700 °C fed by humid H_2 (containing 3 vol% of H_2O). The fuel cell was able to efficiently work at 650 °C in humid H_2 for more than 100 hours without any attenuation. These results indicate that $BaCe_{0.4}Zr_{0.3}In_{0.1}Y_{0.2}O_{3-\delta}$ is a promising electrolyte material for PC-SOFCs.

In future work, fuel cell performance should be further investigated in hydrocarbon gas atmospheres. Novel electrode materials compatible with $BaCe_{0.4}Zr_{0.3}In_{0.1}Y_{0.2}O_{3-\delta}$ should also be investigated.

References

1. Salameh, M.G., *Can renewable and unconventional energy sources bridge the global energy gap in the 21st century?* Applied Energy, 2003. **75**(1-2): p. 33-42.
2. Tesfai, A. and J.T.S. Irvine, *4.10 - Solid Oxide Fuel Cells: Theory and Materials*, in *Comprehensive Renewable Energy*, A. Sayigh, Editor. 2012, Elsevier: Oxford. p. 261-276.
3. Nayyar, Z.A., N.A. Zaigham, and A. Qadeer, *Assessment of present conventional and non-conventional energy scenario of Pakistan.* Renewable & Sustainable Energy Reviews, 2014. **31**: p. 543-553.
4. Wachsman, E.D. and K.T. Lee, *Lowering the Temperature of Solid Oxide Fuel Cells.* Science, 2011. **334**(6058): p. 935-939.
5. Wachsman, E.D., C.A. Marlowe, and K.T. Lee, *Role of solid oxide fuel cells in a balanced energy strategy.* Energy & Environmental Science, 2012. **5**(2): p. 5498-5509.
6. Flipsen, S.F.J., *Power sources compared: The ultimate truth?* Journal of Power Sources, 2006. **162**(2): p. 927-934.
7. Srinivasan, V., *Batteries for Vehicular Applications*, in *Physics of Sustainable Energy: Using Energy Efficiently and Producing It Renewably*, D. Hafemeister, et al., Editors. 2008. p. 283-296.
8. Li, J.-H., et al., *Evaluation of molybdenum carbide as anode catalyst for proton-conducting hydrogen and ethane solid oxide fuel cells.* Electrochemistry Communications, 2012. **15**(1): p. 81-84.
9. Fu, X.-Z., et al., *Ethane dehydrogenation over nano-Cr(2)O(3) anode catalyst in proton ceramic fuel cell reactors to co-produce ethylene and electricity.* Journal of Power Sources, 2011. **196**(3): p. 1036-1041.
10. Fu, X.-Z., et al., *CO2 emission free co-generation of energy and ethylene in hydrocarbon SOFC reactors with a dehydrogenation anode.* Physical Chemistry Chemical Physics, 2011. **13**(43): p. 19615-19623.

11. Fabbri, E., D. Pergolesi, and E. Traversa, *Materials challenges toward proton-conducting oxide fuel cells: a critical review.* Chemical Society Reviews, 2010. **39**(11): p. 4355-4369.

12. Zhou, G.H., et al., *Ag modified LSCF as cathode material for protonic conducting SOFCs.* Materials Technology, 2013. **28**(1-2): p. 3-8.

13. Yan, N., et al., *Ni-P coated Ni foam as coking resistant current collector for solid oxide fuel cells fed by syngas (vol 198, pg 164, 2012).* Journal of Power Sources, 2012. **207**: p. 229-229.

14. Li, J.-H., et al., *Application of BaTiO3 as anode materials for H2S-containing CH4 fueled solid oxide fuel cells.* Journal of Power Sources, 2012. **213**: p. 69-77.

15. Ivanova, M., et al., *Effects of A- and B-site (co-)acceptor doping on the structure and proton conductivity of LaNbO4.* Solid State Ionics, 2012. **213**: p. 45-52.

16. Colantoni, A., et al., *Economical Analysis of SOFC System for Power Production.* Computational Science and Its Applications - Iccsa 2011, Pt Iv, 2011. **6785**: p. 270-276.

17. Kee, R.J., et al., *Modeling the Steady-State and Dynamic Characteristics of Solid-Oxide Fuel Cells.* Advances in Chemical Engineering: Fuel Cell Engineering, Vol 41, 2012. **41**: p. 331-381.

18. Ling, Y., et al., *New ionic diffusion strategy to fabricate proton-conducting solid oxide fuel cells based on a stable La2Ce2O7 electrolyte.* International Journal of Hydrogen Energy, 2013. **38**(18): p. 7430-7437.

19. Schober, T., et al., *The high temperature proton conductor Ba3Ca1.18Nb1.82O9-delta - Part II: electrochemical cell measurements and TEM.* Solid State Ionics, 1999. **118**(3-4): p. 173-178.

20. Wang, J.D., et al., *Protonic conduction in Ca2+-doped La2M2O7 (M = Ce, Zr) with its application to ammonia synthesis electrochemically.* Materials Research Bulletin, 2005. **40**(8): p. 1294-1302.

21. Yamamura, H., H. Nishino, and K. Kakinuma, *Conductivity for Eu2Zr2O7 and La2Ce2O7 with pyrochlore-type composition.* Journal of the Ceramic Society of Japan, 2004. **112**(1310): p. 553-558.

22. Mono, T., et al., *Synthesis and characterization of high temperature proton conductors of type Ba3Ca1+xNb2−xO9−δ.* Ionics, 1995. **1**(5-6): p. 469-473.

23. Valkenberg, S., H.G. Bohn, and W. Schilling, *The electrical conductivity of the high temperature proton conductor Ba3Ca1.18Nb1.82O9-delta.* Solid State Ionics, 1997. **97**(1-4): p. 511-515.

24. Nowick, A.S. and K.C. Liang, *Effect of non-stoichiometry on the protonic and oxygen-ionic conductivity of Sr-2(ScNb)O-6: a complex perovskite.* Solid State Ionics, 2000. **129**(1-4): p. 201-207.

25. Bhella, S.S. and V. Thangadurai, *Synthesis and characterization of carbon dioxide and boiling water stable proton conducting double perovskite-type metal oxides.* Journal of Power Sources, 2009. **186**(2): p. 311-319.

26. Liang, K.C. and A.S. Nowick, *HIGH-TEMPERATURE PROTONIC CONDUCTION IN MIXED PEROVSKITE CERAMICS.* Solid State Ionics, 1993. **61**(1-3): p. 77-81.

27. Nowick, A.S., Y. Du, and K.C. Liang, *Some factors that determine proton conductivity in nonstoichiometric complex perovskites.* Solid State Ionics, 1999. **125**(1–4): p. 303-311.

28. Haugsrud, R., *Defects and transport properties in Ln(6)WO(12) (Ln = La, Nd, Gd, Er).* Solid State Ionics, 2007. **178**(7-10): p. 555-560.

29. Magraso, A., et al., *Development of Proton Conducting SOFCs Based on LaNbO4 Electrolyte - Status in Norway.* Fuel Cells, 2011. **11**(1): p. 17-25.

30. Wang, L., et al., *Investigation on Effect of Sr Doping on Properties of Protonic Conductor La1-xSrxNbO4-sigma.* Chinese Journal of Inorganic Chemistry, 2014. **30**(2): p. 310-316.

31. Mielewczyk-Gryn, A., et al., *Characterization of CaTi0.9Fe0.1O3/La0.98Mg0.02NbO4 composite.* Central European Journal of Physics, 2013. **11**(2): p. 213-218.

32. Labrincha, J.A., J.R. Frade, and F.M.B. Marques, *Protonic conduction in La2Zr2O7-based pyrochlore materials.* Solid State Ionics, 1997. **99**(1-2): p. 33-40.

33. Yamamura, H., et al., *Crystal phase and electrical conductivity in the pyrochlore-type composition systems, Ln(2)Ce(2)O(7) (Ln = La, Nd, Sm, Eu, Gd, Y and Yb).* Journal of the Ceramic Society of Japan, 2003. **111**(12): p. 902-906.

34. Omata, T. and S. Otsuka-Yao-Matsuo, *Electrical properties of proton-conducting Ca2+-doped La2Zr2O7 with a pyrochlore-type structure.* Journal of the Electrochemical Society, 2001. **148**(6): p. E252-E261.

35. Azad, A.K. and J.T.S. Irvine, *Synthesis, chemical stability and proton conductivity of the perovksites Ba(Ce,Zr)(1-x)Sc-x O3-delta.* Solid State Ionics, 2007. **178**(7-10): p. 635-640.

36. Zajac, W., et al., *Applicability of Gd-doped BaZrO3, SrZrO3, BaCeO3 and SrCeO3 proton conducting perovskites as electrolytes for solid oxide fuel cells.* Central European Journal of Chemistry, 2013. **11**(4): p. 471-484.

37. Zayas-Rey, M.J., et al., *Structural and Conducting Features of Niobium-Doped Lanthanum Tungstate, La-27(W1-xNbx)(5)O55.55-delta.* Chemistry of Materials, 2013. **25**(3): p. 448-456.

38. Gill, S., et al., *Effect of Zr substitution for Ce in BaCe0.8Gd0.15Pr0.05O3-delta on the chemical stability in CO2 and water, and electrical conductivity.* Rsc Advances, 2013. **3**(11): p. 3599-3605.

39. Lee, K.-R., et al., *Strontium doping effect on phase homogeneity and conductivity of Ba1-xSrxCe0.6Zr0.2Y0.2O3-delta proton-conducting oxides.* International Journal of Hydrogen Energy, 2013. **38**(25): p. 11097-11103.

40. Kannan, R., et al., *BaCe0.85-xZrxSm0.15O3-delta (0.01 < x < 0.3) (BCZS): Effect of Zr Content in BCZS on Chemical Stability*

in CO2 and H2O Vapor, and Proton Conductivity. Journal of the Electrochemical Society, 2013. **160**(1): p. F18-F26.

41. Ryu, K.H. and S.M. Haile, *Chemical stability and proton conductivity of doped BaCeO3-BaZrO3 solid solutions.* Solid State Ionics, 1999. **125**(1-4): p. 355-367.

42. Bi, L., et al., *Fabrication and characterization of easily sintered and stable anode-supported proton-conducting membranes.* Journal of Membrane Science, 2009. **336**(1-2): p. 1-6.

43. Fabbri, E., et al., *Towards the Next Generation of Solid Oxide Fuel Cells Operating Below 600 degrees C with Chemically Stable Proton-Conducting Electrolytes.* Advanced Materials, 2012. **24**(2): p. 195-208.

44. Rahman, S.M.H., et al., *50 mol% indium substituted BaTiO3: Characterization of structure and conductivity.* International Journal of Hydrogen Energy, 2012. **37**(9): p. 7975-7982.

45. Katahira, K., et al., *Protonic conduction in Zr-substituted BaCeO3.* Solid State Ionics, 2000. **138**(1-2): p. 91-98.

46. Shimada, T., et al., *The high temperature proton conductor BaZr0.4Ce0.4In0.2O3-alpha.* Journal of Power Sources, 2004. **131**(1-2): p. 289-292.

47. Sawant, P., et al., *Synthesis, stability and conductivity of BaCe0.8-xZrxY0.2O3-delta as electrolyte for proton conducting SOFC.* International Journal of Hydrogen Energy, 2012. **37**(4): p. 3848-3856.

48. Della Negra, M., et al., *Behavior of BaCe0.9-x Zr (x) Y0.1O3-delta in water and ethanol suspensions.* Journal of Materials Science, 2014. **49**(6): p. 2588-2595.

49. Iijima, M., et al., *Cell performance stability of HNIFC using Ba(Ce1-xZrx)0.8Y0.2O3 perovskite type proton conductor as electrolyte*, in *Solid-State Ionics-2006*, E. Traversa, et al., Editors. 2007. p. 45-53.

50. Fabbri, E., et al., *Tailoring the chemical stability of Ba(Ce0.8-xZrx)Y0.2O3-delta protonic conductors for Intermediate*

Temperature Solid Oxide Fuel Cells (IT-SOFCs). Solid State Ionics, 2008. **179**(15-16): p. 558-564.

51. Lim, D.K., et al., *Partial conductivities of mixed conducting BaCe0.65Zr0.2Y0.15O3-delta.* International Journal of Hydrogen Energy, 2010. **35**(19): p. 10624-10629.
52. Yan, L., et al., *Influence of fabrication process of Ni-BaCe0.7Zr0.1Y0.2O3-delta cermet on the hydrogen permeation performance.* Journal of Alloys and Compounds, 2010. **508**(1): p. L5-L8.
53. Zuo, C.D., et al., *Ba(Zr0.1Ce0.7Y0.2)O3-delta as an electrolyte for low-temperature solid-oxide fuel cells.* Advanced Materials, 2006. **18**(24): p. 3318-+.
54. Guo, Y.M., et al., *Zirconium doping effect on the performance of proton-conducting BaZryCe0.8-yY0.2O3-delta (0.0 <= y <= 0.8) for fuel cell applications.* Journal of Power Sources, 2009. **193**(2): p. 400-407.
55. Yang, L., et al., *Enhanced Sulfur and Coking Tolerance of a Mixed Ion Conductor for SOFCs: BaZr0.1Ce0.7Y0.2-xYbxO3-delta.* Science, 2009. **326**(5949): p. 126-129.
56. Ngoc Thi Quynh, N. and H.H. Yoon, *Preparation and evaluation of BaZr0.1Ce0.7Y0.1Yb0.1O3-delta (BZCYYb) electrolyte and BZCYYb-based solid oxide fuel cells.* Journal of Power Sources, 2013. **231**: p. 213-218.
57. Fabbri, E., et al., *Chemically Stable Pr and Y Co-Doped Barium Zirconate Electrolytes with High Proton Conductivity for Intermediate-Temperature Solid Oxide Fuel Cells.* Advanced Functional Materials, 2011. **21**(1): p. 158-166.
58. Bi, L., et al., *Sinteractivity, proton conductivity and chemical stability of BaZr0.7In0.3O3-delta for solid oxide fuel cells (SOFCs).* Solid State Ionics, 2011. **196**(1): p. 59-64.
59. Li, X., et al., *Synthesis and electrical properties of Co-doped Y0.08Sr0.92TiO3 − δ as a potential SOFC anode.* Solid State Ionics, 2008. **179**(27–32): p. 1588-1592.
60. Barison, S., et al., *High conductivity and chemical stability of BaCe(1-x-y)Zr(x)Y(y)O(3-delta) proton conductors prepared*

by a sol-gel method. Journal of Materials Chemistry, 2008. **18**(42): p. 5120-5128.

61. Bi, L., et al., *Indium as an ideal functional dopant for a proton-conducting solid oxide fuel cell.* International Journal of Hydrogen Energy, 2009. **34**(5): p. 2421-2425.
62. Zhao, F., et al., *Novel BaCe0.7In0.2Yb0.1O3-delta proton conductor as electrolyte for intermediate temperature solid oxide fuel cells.* Journal of Power Sources, 2011. **196**(18): p. 7500-7504.
63. Tao, S.W. and J.T.S. Irvine, *A stable, easily sintered proton-conducting oxide electrolyte for moderate-temperature fuel cells and electrolyzers.* Advanced Materials, 2006. **18**(12): p. 1581-+.
64. Amsif, M., et al., *Effect of sintering aids on the conductivity of BaCe0.9Ln0.1O3−δ.* Journal of Power Sources, 2011. **196**(22): p. 9154-9163.
65. Kim, D.-H., B.-K. Kim, and Y.-C. Kim, *Effect of zinc oxide as a sintering aid on proton migration across Sigma 5 (310)/ 001 tilt grain boundary of barium zirconate.* Journal of Electroceramics, 2013. **30**(1-2): p. 19-23.
66. Lu, Z., et al., *Performance of anode-supported solid oxide fuel cell with thin bi-layer electrolyte by pulsed laser deposition.* Journal of Power Sources, 2012. **210**: p. 292-296.
67. Daneshmandi, S., et al., *Effect of oxygen pressure on structural and electrical properties of Ba0.5Sr0.5Co0.8Fe0.2O3-delta/SrTiO3(200) by reactive pulsed laser deposition.* Materials Letters, 2013. **109**: p. 233-236.
68. Mukai, T., et al., *Fabrication of Y2O3-Doped Zirconia/Gadolinia-Doped Ceria Bilayer Electrolyte Thin Film SOFC Cells of SOFCs by Single-Pulsed Laser Deposition Processing.* Journal of Fuel Cell Science and Technology, 2013. **10**(6).
69. Saporiti, F., et al., *Yttria and Ceria Doped Zirconia Thin Films Grown by Pulsed Laser Deposition.* Materials Research-Ibero-American Journal of Materials, 2013. **16**(3): p. 655-660.

70. Bobrenok, O.F. and M.R. Predtechenskii, *Solid Oxide Fuel Cells with Film Electrolytes Prepared by Chemical Vapor Deposition.* Russian Journal of Electrochemistry, 2010. **46**(7): p. 798-804.

71. Schlupp, M.V.F., et al., *Thin film growth of yttria stabilized zirconia by aerosol assisted chemical vapor deposition.* Journal of Power Sources, 2012. **202**: p. 47-55.

72. Schlupp, M.V.F., et al., *Gadolinia Doped Ceria Thin Films Prepared by Aerosol Assisted Chemical Vapor Deposition and Applications in Intermediate-Temperature Solid Oxide Fuel Cell.* Fuel Cells, 2013. **13**(5): p. 658-665.

73. Marichy, C., M. Bechelany, and N. Pinna, *Atomic Layer Deposition of Nanostructured Materials for Energy and Environmental Applications.* Advanced Materials, 2012. **24**(8): p. 1017-1032.

74. Magraso, A., et al., *Novel Fabrication of Ca-Doped LaNbO4 Thin-Film Proton-Conducting Fuel Cells by Pulsed Laser Deposition.* Journal of the American Ceramic Society, 2010. **93**(7): p. 1874-1878.

75. Chao, C.-C., et al., *Improved Solid Oxide Fuel Cell Performance with Nanostructured Electrolytes.* Acs Nano, 2011. **5**(7): p. 5692-5696.

76. Giannici, F., et al., *Indium Doping in Barium Cerate: the Relation between Local Symmetry and the Formation and Mobility of Protonic Defects.* Chemistry of Materials, 2007. **19**(23): p. 5714-5720.

77. Lefebvre-Joud, F., G. Gauthier, and J. Mougin, *Current status of proton-conducting solid oxide fuel cells development.* Journal of Applied Electrochemistry, 2009. **39**(4): p. 535-543.

78. Amsif, M., et al., *Influence of rare-earth doping on the microstructure and conductivity of BaCe0.9Ln0.1O3−δ proton conductors.* Journal of Power Sources, 2011. **196**(7): p. 3461-3469.

79. Sawant, P., et al., *Synthesis, stability and conductivity of BaCe0.8−xZrxY0.2O3−δ as electrolyte for proton conducting*

SOFC. International Journal of Hydrogen Energy, 2012. **37**(4): p. 3848-3856.

80. Chi, X., et al., *Influence of In doping on the structure, stability and electrical conduction behavior of Ba(Ce,Ti)O-3 solid solution.* Journal of Alloys and Compounds, 2013. **554**: p. 378-384.

81. Liu, Y., et al., *A novel approach for substantially improving the sinterability of BaZr04Ce0.4Y0.2O3-delta electrolyte for fuel cells by impregnating the green membrane with zinc nitrate as a sintering aid.* Journal of Membrane Science, 2013. **437**: p. 189-195.

82. Luisetto, I., et al., *Electrochemical performance of spin coated dense BaZr0.80Y0.16Zn0.04O3-delta membranes.* Journal of Power Sources, 2012. **220**: p. 280-285.

83. Kjølseth, C., et al., *Space–charge theory applied to the grain boundary impedance of proton conducting BaZr0.9Y0.1O3 – δ.* Solid State Ionics, 2010. **181**(5–7): p. 268-275.

84. Fleig, J., et al., *Inhomogeneous current distributions at grain boundaries and electrodes and their impact on the impedance.* Solid State Ionics, 1998. **113–115**(0): p. 739-747.

85. Shimada, H., et al., *Proton-Conducting Solid Oxide Fuel Cells with Yttrium-Doped Barium Zirconate for Direct Methane Operation.* Journal of the Electrochemical Society, 2013. **160**(6): p. F597-F607.

86. Hirschorn, B., et al., *Determination of effective capacitance and film thickness from constant-phase-element parameters.* Electrochimica Acta, 2010. **55**(21): p. 6218-6227.

87. Giannici, F., et al., *Dopants and defects: Local structure and dynamics in barium cerates and zirconates.* Solid State Ionics, 2010. **181**(3-4): p. 122-125.

88. Sun, W., et al., *Chemically stable and easily sintered high-temperature proton conductor BaZr0.8In0.2O3-delta for solid oxide fuel cells.* Journal of Power Sources, 2013. **229**: p. 95-101.

89. Singhal, S.C., *Science and Technology of Solid-Oxide Fuel Cells.* MRS Bulletin, 2000. **25**(03): p. 16-21.

90. Yoo, Y. and N. Lim, *Performance and stability of proton conducting solid oxide fuel cells based on yttrium-doped barium cerate-zirconate thin-film electrolyte.* Journal of Power Sources, 2013. **229**: p. 48-57.